IISc Theses Abstracts

Contents

J. Indian Inst. Sci., Nov–Dec 1993, **73**, 599–654.

IISc THESES ABSTRACTS

Thesis Abstract (Ph.D.)

Design, fabrication and instrumentation of a broadcast bus multicomputer system by M. P. Srinivasan
Research supervisors: V. Rajaraman and E. S. Rajagopal
Department: Instrumentation and Services Unit

1. Introduction

The quest for higher performance and more reliable computers at lower costs goes on relentlessly. The future generation of computers are expected to handle far more complex systems, go beyond handling numbers and become capable of processing voice and pictures, run fully automated factories, communicate with humans interactively through speech and images, etc. It is recognised that the next generation of computers are intelligent and knowledge-based systems, while taking advantage of the full power of device technology, will require new approaches to systems architecture With the advent of efficient microcomputers, interest in building large multicomputer structures has grown considerably over the last few years[1] Two main directions in research can be identified: (i) to build a general-purpose multicomputer by interconnecting a large number of microcomputers, and (ii) to build a special-purpose machine suited for a specific environment. In both the cases, interconnection for communication is an important part of research[2]. Multicomputer systems represent an important opportunity for novel architectural approaches in building computing systems to better suit a given application requirement initially and also to adapt to changes during the system's life cycle.

2. Proposed architecture

The broadcast bus multicomputer system (BBMS) is an improved message-passing multicomputer based on a custom-designed, time-shared bus called message broadcast bus (MBB). This architecture has a number of enhancements over the conventional message-passing multicomputer systems[3] The major improvements are:

- Reduction in inter-processor communication overhead by providing a high-speed communication controller implemented using programmable logic devices.
- A high-speed hardware circuit to match the destination address on fly.
- A dynamically programmable match store
- Facility to receive messages which are out of sequence.
- A new fair arbitration scheme.
- Modular hardware design for future upgradation.
- A programmable instrumentation module for tuning the system

3. System organisation

The BBMS consists of the following subsystems:

- A set of nodes, called the computing elements (CEs), consisting of an instruction processor, a floating point processor, two identical communication units and local memory.

- Two high-speed parallel data transfer broadcast buses called message broadcast bus (MBB).
- A centralised bus arbiter with parallel request inputs and parallel grant outputs.
- A host computer which generates the task graph and maps it on to the computing elements.
- An instrumentation module.

The main function of the CE is to execute the code of the assigned task and send the computed results to its successors as defined by the task graph The generation of the task graph and scheduling of the tasks on the CEs form the function of the host computer. Inter-processor communication is in the form

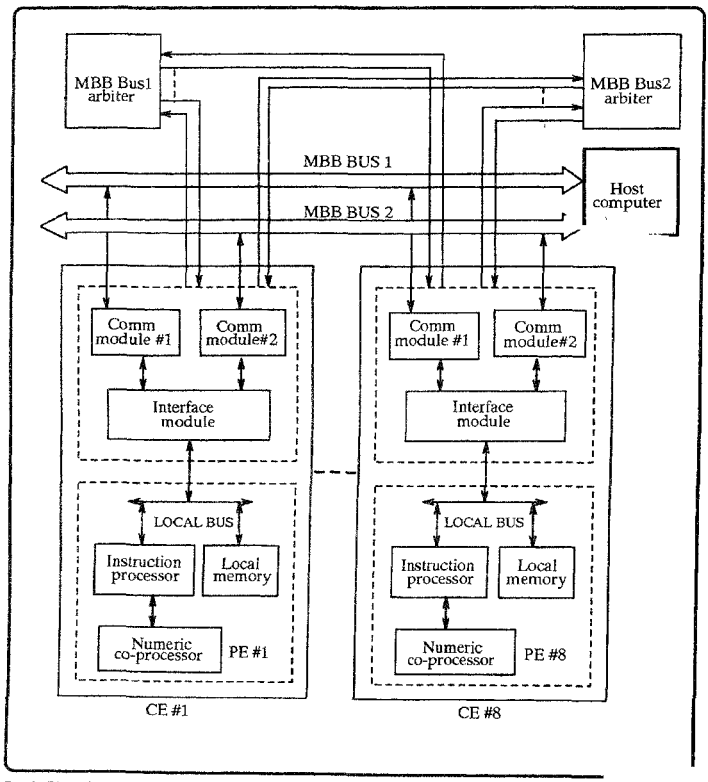

FIG. 1 Block diagram of BBMS

of packets *via* the bus. The communication subsystem is responsible for obtaining access to the bus. It also supports point-to-point, multicast and broadcast protocols.

The two message broadcast buses interconnect all the computing elements of the system with equal opportunity for all the CEs to use either of the buses for message transfer. The advantage of dual bus is that it provides an alternative path in case of a fault in one of the buses and doubles the message traffic handling capability. The two buses can also be used separately for system and application program communication requirements, thereby eliminating system deadlocks caused by bugs in the application programs.

The bus arbiter revolves the bus requests by the CEs and allocates the bus with a predetermined allocation policy. The arbiter is designed using high-speed logic-minimizing arbitration time. It has a unique feature of gating the requests periodically and completing the bus allocation before gating the next set of requests. This prevents any CE from monopolizing the bus indefinitely.

An instrumentation system is designed and interfaced with BBMS (Fig. 1) to gain insight into the system's activities, detect and analyse bottlenecks, and to obtain qualitative and quantitative assessments. This instrumentation is also useful to understand the parallel activities, their effect on the performance of the algorithm or the processor, and causes for special or unusual behaviour. This is more important when the machine is not performing as expected.

4. Conclusions

An 8-CE multicomputer system is built using the above ideas The processing elements are 80386 single board computers. Extensive diagnostic tests are run on the system to study the reliability of the system. Parallel algorithms are developed for a few selected popular applications like sorting, matrix multiplication, median filtering for image processing, PDE, etc. These programs are executed on the system and performance measures are collected. Based on these measurements, design issues like application-dependent architectures, communication bottlenecks, arbitration policies, load balancing, etc., are studied

References

1. HWANG, K. AND BRIGGS, F. A — *Computer architecture and parallel processing*, 1984, McGraw-Hill
2. STONE, S. H — *High-performance computer architecture*, 1987, Addison-Wesley
3 REED, A. D. AND FUJIMOTO, M. R — *Multicomputer networks*, 1987, MIT Press.

Thesis Abstract (Ph.D.)

A study of the implementation of speculative parallelism in functional languages by P. V. R. Murthy
Research supervisor: V. Rajaraman
Department: Computer Science and Automation

1. Introduction

With the goal of minimising execution times of programs, a lot of work has been done and is under way to execute programs in parallel. Two approaches were employed to execute programs written in imperative languages in parallel. They are: (a) providing explicit constructs to express parallelism, and (b) letting a compiler detect parallelism in a program written for a sequential machine. In approach (a), the burden of synchronization and partitioning the program is on the programmer. In approach (b), the burden of detecting parallelism in a sequential program is on a compiler. Automatic detection of parallelism in a sequential program is quite hard. Though commendable progress is made in this direction, there are basic limitations with the approach as the attempt is to parallelize an inherently sequential program.

Functional languages[1,2] have gained wide attention recently because of several advantages that they offer over conventional languages. Programs written in these languages satisfy the Church–Rosser property[3] and as a result the order of evaluation of sub-expressions in an expression is irrelevant for the final result (however, some reduction sequences may not terminate). The above property makes functional languages an attractive choice for parallel evaluation. However, it may be noted that if a functional program is based on a sequential algorithm, its evaluation does not generate parallelism. Thus, the creative work of a programmer to invent a parallel algorithm is still needed. Lazy evaluation based on normal order reduction is usually employed to evaluate functional programs because it aids in the modularization of programs[4]. Efforts were made to increase concurrency in a lazy implementation[5,6]. Burton[7] proposes methods to employ speculation in problems involving parallel search. More recently, Osborne addresses the problem of speculative computation in Multilisp[8].

It is reported in the literature that about half of lambda abstractions are non-strict. This work addresses the problem of identifying useful speculative parallelism in a functional program, methods to implement it and identifies the necessary conditions that a program needs to satisfy for speculative evaluation to perform better than lazy evaluation.

2. Parallelism in functional programs

Parallelism in functional programs may be broadly classified as (a) conservative parallelism, and (b) speculative parallelism. In the conservative parallelism scheme, only those expressions which are certainly known to be necessary for a program's evaluation are scheduled ahead for evaluation before their results are actually demanded. In the speculative parallelism scheme, even those expressions whose results may or may not be needed for a program's evaluation are scheduled for evaluation ahead before they are actually known to be necessary. For programs which do not generate sufficient conservative parallelism to keep all the processors in a system busy, it is worth attempting speculative evaluation so that the spare processors are not idle. But an important question to be answered is—how best may the spare processors be used? A naive approach is to speculatively evaluate any expression that possibly can be reduced not taking into account its degree of utility. A more intelligent speculative scheme would be to identify expressions that have a greater degree of utility on an average and speculatively schedule only such expressions for evaluation. Uncertainty about which expressions are needed for a user-defined function's evaluation is mainly due to if-then-else expressions. Branch probability is the probability with which the condition in an if-then-else expression evaluates to true. If branch probabilities are available either through measurement or user annotations, it would be possible for a system to identify expressions of greater utility. Most of the functions in functional programs are defined recursively. During the evaluation of a recursive function application, it is the recursive arm that is selected for evaluation more often than the terminating arm. Thus, even if branch probabilities were not measured, it is reasonable if the programmer specifies that the probability of selection of the recursive arm is much greater than that of the terminating arm.

3. Models of speculative evaluation

Two speculative evaluation models are proposed in this work. They are: (a) branch speculation, and (b) argument speculation. In branch speculation, the more promising branch in an if-then-else expression is evaluated in parallel with the condition. Priorities are assigned to tasks executing expressions and these are directly proportional to the probabilities with which expressions are required for a program's evaluation. In argument speculation, the attempt is to reduce promising non-strict arguments in parallel with the strict arguments and the body of a user-defined function. In both the speculation models, components of a list structure are evaluated lazily.

To be able to detect promising non-strict arguments, we have developed an analysis technique to quantify the strictness of a function in each of its arguments.

4. Quantification of strictness

The minimum information that a compiler requires to quantify the strictness of a function in each of its arguments is the branch probability in each if-then-else expression. We first show how to compute the

probability with which a primitive expression requires a given variable for its evaluation A primitive expression may be (a) a constant, (b) a variable, (c) a strict built-in function application, (d) an if-then-else expression, (e) an expression of the form e1:e2, (f) (not e) or (−e) and (g) (hd e) or (tl e). The rules developed for primitive expressions are used to compute the probability with which a user-defined function requires an argument To handle recursive functions, a successive approximation method is used. The method is extended to higher order functions too.

5. Evaluation based on speculation

We have designed a functional language to experiment with the ideas mentioned already. The language consists of all the essential features of functional languages. A compiler is developed to translate programs written in the language into prefix graphs. We have simulated an MIMD multiprocessor with shared memory. We have run a number of programs using the simulated multiprocessor varying the number of processors from 4 to 64.

Lazy and speculative evaluations based on branch and argument speculations, and eager evaluation are implemented using an interpretive model of graph reduction Speculative evaluation based on both static and dynamic priorities is implemented. The issues in task priority upgradation and irrelevant task deletion are addressed. By running each program several times with random inputs, we have compared lazy and eager evaluation times with speculative evaluation. Overheads due to speculation and wastage due to speculation are measured.

6. Conclusions

Based on our simulation studies, we have arrived at the following conclusions Programs which satisfy the following conditions are evaluated faster using speculation with static priorities than lazy evaluation, reducing the evaluation time even by about 20%. The conditions are: (a) the conservative parallelism in a program cannot keep all the processors in a system busy, and (b) the time that a lazy evaluator may take to detect the actual necessity of a promising branch or a promising non-strict argument is significant. Speculation with dynamic priorities results in considerable overheads. We have also observed that argument speculation performs better than eager evaluation if there exist non-strict arguments with both high and low probabilities of requirement and the low priority arguments can generate substantial parallelism. On the other hand, if all non-strict arguments of a function are needed with high probabilities for the function's evaluation, then eager evaluation performs slightly better than speculative evaluation.

References

1. Backus, J. — Can programming be liberated from the Von Neumann style? A functional style and its algebra of programs, *Commun. ACM*, 1978, **21**, 613–641.
2. Hudak, P — Conception, evolution and application of functional programming languages, *ACM Computing Surv.*, 1989, **21**, 359–411.
3 Peyton-Jones, S. L — *The implementation of functional programming languages*, 1987, Prentice-Hall
4. Hughes, J. — Why functional programming matters?, *Comput J*, 1989, **32**, 98–107
5. Clack, C. and Peyton-Jones, S. L — A practical approach to strictness analysis In *Functional programming languages and computer architecture, Lecture Notes in Computer Science* 201, pp. 190–203, 1985, Springer–Verlag.
6. Burn, G L. — *Evaluation transformers. A model for the parallel evaluation of functional languages, Lecture Notes in Computer Science* 274, pp. 446–469, 1987, Springer–Verlag.
7. Burton, F. W. — Speculative computation, parallelism, and functional programming, *IEEE Trans.*, 1985, **C-34**, 1190–1193
8. Osborne, R. B. — *Speculative computation in Multilisp, Parallel Lisp : Languages and Systems, Lecture Notes in Computer Science* 441, pp 103–137, 1989, Springer–Verlag

Thesis Abstract (M.Sc. (Engng))

Transputer-based parallel implementation of neural nets for a class of pattern recognition problems by Indu Mahadevan
Research supervisor: L. M. Patnaik
Department: Computer Science and Automation

1. Introduction

Artificial neural nets (ANNs) have been studied in the hope of achieving human-like performance in the fields of speech and image recognition[1]. ANNs are biologically inspired and exhibit a number of brain functions. Neural networks have been used in various fields of pattern recognition. ANNs attempt to achieve good performance *via* dense interconnections of simple computational elements[2]. The dense interconnections between the layers in a network and the fact that all neurons in any particular layer of the network can work in parallel make ANNs highly amenable to parallel implementation.

2. An overview of the work

The work presented concerns with the parallel implementation and performance evaluation of two neural net models, bidirectional associative memory (BAM) and backpropagation. BAM has been simulated on transputer-based topologies like hypercube, mesh and linear array and speedup and utilization of these topologies has been found. A condition for multiple training of BAM for many patterns has been derived. Dummy data augmentation method has been tried for storing more data in the network. Backpropagation network has been implemented on linear array and ring topologies. Both the networks have been used for numeral recognition. Backpropagation network has been used in medicine to diagnose various kinds of arthritis.

3. Transputers for simulation of neural networks

A transputer is a microcomputer with its own local memory and high-speed communicating links for connecting one transputer to another hence making it easy to build various topologies. ANNs belong to a general class of communicating sequential processes (CSP)[3]. Occam language and transputers efficiently implement CSP making ANN development and testing easier. Neural networks are also suitable for parallel implementation and the transputer serves as a good platform for simulation.

4. Parallel implementation of BAM and backpropagation networks

BAM and backpropagation networks have been implemented on various transputer-based topologies.

4.1. *Parallel implementation of BAM*

BAM is a two-layered feedback neural net used for pattern recognition in a noisy environment[4]. BAM operations mainly involve vector–matrix multiplications and are compute-intensive in nature, making it suitable for parallel implementation.

BAM is simulated on topologies like hypercube, mesh and linear array. Hypercube topology gives a better speedup and utilization when compared to mesh and linear array since the problem can be mapped on to the topology in such a way that smaller diameter of a topology is made use of to reduce communication time between processors (Fig. 1). The speedup obtained when the number of transputers is increased is not linear because communication time keeps increasing. Utilization of the system drops as the number of transputers increases because communication time starts increasing with the computation time remaining the same (Fig. 2).

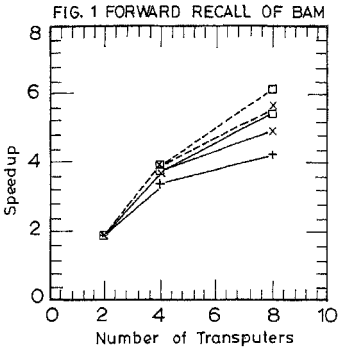

FIG. 1. Forward recall of BAM
+ Linear array, × Mesh, □ Hypercube.

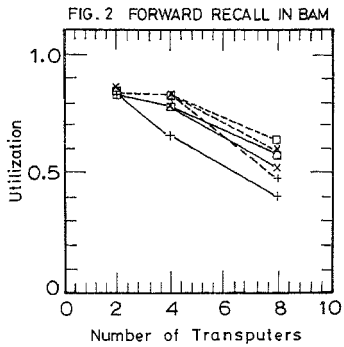

FIG 2 Forward recall in BAM
---- Without setup time, —— With setup time. Neurons per layer. 80

4.2. *Parallel implementation of backpropagation network*

Backpropagation is a supervised learning technique used for training multilayer ANNs[5]. This technique is useful in areas of image and speech processing, etc. The processes of learning and recalling in a backpropagation network are compute-intensive and are amenable to parallel implementation. All neurons in any particular layer operate in parallel and can be mapped on to various transputers for parallel operation. The network has been implemented on a linear array and ring of transputers. The number of transputers is varied and the speedup obtained. The two-transputer version is closer to its theoretical maximum speedup of two when compared to the four- and eight-transputer versions because of lesser communication. Linear array performs better during recalling of patterns because the sending of parameters between the transputers is done less frequently and in larger packets. In the case of learning, the ring topology is better since the process involves a lot of communication with the host and the smaller diameter of the ring topology makes it faster.

5. Numeral recognition on BAM and backpropagation networks

BAM and backpropagation networks are used for numeral recognition. BAM has a limited storage capacity and the concepts of multiple training and dummy data augmentation are used to improve the storage capacity. The number of patterns that could be stored in BAM depends on how the patterns are coded.

5.1. *Multiple training in BAM*

The number of patterns that can be stored in BAM and can be recalled perfectly can be altered using multiple training[6]. Recalling of any one pattern can be guaranteed with adequate number of trainings called multiplication factor. If an arbitrary number of patterns have to be recalled perfectly, there is no way to guarantee the recall of all the patterns.

To achieve perfect recall of any i patterns, $x_1, x_2, \ldots x_i$, we must find i values of multiplication factors, mult1, mult2, . . . multi in such a way that the following condition is satisfied for every element n in the i patterns.

$$\text{Sign (multa * multa * } (x_a * x_a^T) * x_{am}) = \text{Sign (multa * multb * } (x_a * x_b^T) * x_{bn})$$

where x_{im} represents the mth position in pattern x_i.

If the patterns are autoassociated, multiplication factors are found for either input or output pattern sets, else it must be found for both the set of input and output patterns. The resultant set of multiplication factors represents the maximum of the two sets of multiplication factors obtained.

5.2. *Dummy data augmentation*

Dummy data augmentation method guarantees the recall of all training pairs provided the right amount of dummy sets are augmented to the patterns while training and recalling[6] With dummy data augmentation, all the ten numerals can be stored on BAM.

5.3. *Simulation results*

BAM network in general has less storage capacity. Recalling capability depends on the pattern to be classified. With multiple training and dummy data augmentation, the capacity was increased. Dummy data augmentation method classifies better in the presence of noise when compared to the network trained using multiple training method. The backpropagation network is able to withstand noise to quite an extent and classifies better than the BAM network.

6. Medical diagnosis using backpropagation network

Neural nets are playing an important role in diagnosis and treatment because of their properties of experience-based learning, fault tolerance and graceful degradation[7]

Backpropagation network is used in the field of medicine. The network has been used to diagnose various kinds of arthritis and allied rheumatic disorders classified as patterns. Various parameters of the joint fluid are measured and fed into the network to recognize seven of the major types of arthritis and allied rheumatic disorders. To simulate a physician's reasoning as closely as possible, the system has been divided into modules, one for each parameter. Each hidden layer represents a module The network has been implemented on a linear array of four transputers giving a speedup of 2.89 when compared to a single transputer implementation.

7. Conclusions

Transputer-based parallel implementation of BAM and backpropagation network give good speedup. Hypercube topology is better in terms of speedup and utilization in implementing BAM. Ring topology performs better during learning and linear array performs better during recalling operations in backpropagation network. Numeral recognition on backpropagation network is better than on BAM in the presence of noise. Multiple training and dummy data augmentation improve BAM-recalling capabilities. Arthritis diagnosis on backpropagation network shows promising trends for future implementation.

References

1.	ANDERSON, J A. AND ROSENFELD, E.	*Neurocomputing foundations of research*. 1988, MIT Press
2.	LIPPMANN, R P	An introduction to computing with neural nets, *IEEE ASSP Mag* , 1987, 2, 4–22.
3.	KOIKKALAINEN, P. AND OJA, E	Specification and implementation environment for neural networks using communicating sequential processes, *IEEE ICNN*, 1987, I-533–I-540
4.	KOSKO, B	Adaptive bidirectional associative memories, *Appl. Opt.*, 1987, **26**, 4947–4960
5	RUMELHART, D. E., HINTON, G. E. AND WILLIAMS, R. J	Learning representations by backpropagating errors, *Nature*, 1986, **323**, 533–536
6.	WANG, Y. F. *et al*	Two coding strategies for BAM, *IEEE Trans.*, 1990, **NN-1**, 81–92.
7.	POLI, R *et al*	A neural network expert system for diagonising and treating hypertension, *IEEE Comput.*, 1991, **24**, 64–71

Thesis Abstract (Ph.D.)

Knowledge teaching: An alternative strategy for knowledge-base development by
Mohsen Sadighi Moshkenani
Research supervisor: V. V. S. Sarma
Department: Computer Science and Automation

1. The problem

In the development of knowledge-based systems, human expertise or his knowledge of a specific domain is sought to be transferred to the knowledge-base of such expert systems. The process of this transfer is termed knowledge acquisition or knowledge elicitation and this has been recognized as a very difficult and time-consuming task 'the knowledge-acquisition bottleneck'. In literature, the classical paradigm for this transfer is through an intermediary called the 'knowledge engineer' which is substituted by automatic knowledge-acquisition programs in more recent systems.

2. Approach

Here, we approach the problem of knowledge acquisition as an educational activity, with the domain expert taking the role of a conventional teacher, attempting to transfer his expertise, *via* a computer program called the expertise-student program, to develop the knowledge-base.

3. Motivation

The present work was motivated by the observation that knowledge acquisition, and, in fact, any knowledge transfer, by definition, intuition, and nature, is an educational activity. Moreover, current knowledge-acquisition techniques, as obvious from their generic name, are based on extraction, elicitation and generally acquisition of knowledge from knowledge sources (usually human experts). In these techniques, the receiver of knowledge (a knowledge engineer, or an automatic knowledge-acquisition system), specifies what should be acquired and when; which could be recognized as student-oriented educational methods (such as self-study or apprenticeship) in analogy with the education metaphor. In contrast, the bulk of the human knowledge transfer is *via* teachers, or in other words, human education is teacher oriented

4. Objective

In this work, we investigate the feasibility of using a general teaching strategy, and its associated development environment. Our objective is to use domain experts to be denoted expertise-teachers who are also familiar with education, to teach domain knowledge, which is necessary and sufficient for developing the required knowledge-base. The receiver of this knowledge (the student) is a program called the 'expertise–student program', which collects the entered knowledge, transfers it to an appropriate internal form and uses it for further interactions (such as query answering). At this stage, from the view point of the expertise-teacher, this process would be somewhat similar to the education of mentally retarded students; because he should consider the debilities of the expertise-student program. He should try for clear and specific decomposition of the knowledge to be entered, to available and understandable knowledge forms of the expertise-student program.

5. Organization

The work starts with the main concepts involved in this investigation; knowledge, knowledge-base, knowledge-based system, knowledge acquisition, knowledge and its distinction from information and data. The concept of nonuniformity of knowledge is considered because of its major role in any knowledge processing. Reasons for knowledge-acquisition bottleneck are also reviewed.

We observe that knowledge acquisition, like any knowledge-transfer process, is an educational activity. Then, using major factors of any educational activity such as its goal, the student, and the teacher characteristics and the method, key issues of knowledge acquisition are presented. An interesting point regarding

the use of the education metaphor is that it shows some key points regarding knowledge, and knowledge acquisition, which are not fully appreciated in literature. The amount of contribution of the source and destination parts in the knowledge-transfer process are used as a basis for a classification of the current knowledge-acquisition techniques. It is concluded that the current knowledge-acquisition techniques are predominantly student oriented in spite of human experience in education which is essentially teacher oriented.

Subsequently, incorporating the wealth of human experience in education, the knowledge-teaching paradigm as an alternative strategy for transfering human knowledge to knowledge-bases is introduced, and its major issues are discussed, including the characteristics/duties of expertise-teacher and expertise-student program; the type of knowledge to be transferred and the role of the relevant domains; the managerial role of the knowledge engineer, the development life cycle of the knowledge-based systems *via* the knowledge-teaching paradigm and the new problems which should be resolved.

We also study the contribution of the knowledge-teaching paradigm in making expert system technology more efficient by finding its impact on the development life cycle of knowledge-based systems and removing or decreasing various bottlenecks, like brittleness. In other words, the knowledge-teaching approach is evaluated based on some criteria which are fixed first.

The specifications and the design issues of the expertise-student program are considered. Based on these considerations, a sample architecture is proposed. Special modules for representing and using each form of knowledge and differences between expertise-student program and the conventional knowledge-acquisition tools are also noted.

We also report on the development of a prototype expertise-student program (ESP) involving the operationalization of the knowledge-teaching paradigm. After a general description of its external behaviour, its technical specifications about representation and utilization of each one of its knowledge forms, and its general procedure of reasoning are presented.

Finally, we present an application of ESP, in developing a tutoring system, with different categories of knowledge (pedagogical knowledge, domain knowledge, and the knowledge-entered through the knowledge engineer) from different sources. The report includes several practical problems encountered in the implementation phase.

References

1. BOOSE, J. H. — A survey of knowledge acquisition techniques and tools, *Knowledge Acquisition*, 1980, **1**, 3–37.
2. DAVIS, R. AND BUCHANAN, B. G. — Meta-level knowledge. In *Rule-based expert systems* (B G Buchanan and E H. Shortliffe (eds)), pp. 507–530, 1984, Addison–Wesley
3. DAVIS, R AND LENAT, D. B. — *Knowledge-based systems in artificial intelligence*, 1982, McGraw-Hill.
4. DHALIWAL, J. S. AND BENBASAT, I. — A framework for the comparative evaluation of knowledge acquisition tools and techniques, *Knowledge Acquisition*, 1990, **2**, 145–166
5. GAINES, B R. — An overview of knowledge-acquisition and transfer, *Int. J Man–Mach. Stud.*, 1987, **26**, 453–472.
6. GAINES, B. R. — Knowledge acquisition systems for rapid prototyping of expert systems, *INFOR*, 1988, **26**, 256–285.

Thesis Abstract (Ph.D.)

Acoustic emission signal analysis: An unsupervised pattern recognition approach by M. Abdul Majeed

Research supervisor: C. R. L. Murthy

Department: Aerospace Engineering

1. Introduction

The term 'acoustic emission' (AE) strictly refers to the phenomenon by which pressure waves are generated in a material by the rapid release of energy from dynamic processes such as crack growth. The pressure

waves so generated are also commonly referred to in the literature as acoustic emission. The vital information contained in these waves can be extracted and analysed to characterize the defects and assess their severity. The analysis for this purpose is facilitated by conversion of the pressure waves into electrical signals called AE signals. Though the potential of AE as an 'active' NDE method has long been recognised, its use is limited to simple applications such as pressure vessel monitoring and leak detection. Its application to more complex problems like inflight monitoring has not exactly been successful mainly because of the lack of an appropriate signal analysis methodology.

The major problem in AE signal analysis relates to: (1) separation of true AE from pseudo-AE and AE-like noises, and (2) classification of signals of distinct origins. Though some recent researchers have advocated the use of statistical pattern recognition (PR) or pattern classification as a solution to this problem, most of these investigations appear to be feasibility studies carried out using conventional PR techniques on simple problems. Thus, the stated problem, *i.e.*, sorting signal and noise, and classification of signals for purposes of NDE utilizing AE, is so complex in nature that an indepth study is required for its solution. This has provided us the major impetus for carrying out the work reported here.

2. Studies on feature extraction

A PR process consists of two major subprocesses: feature extraction and classification[1]. The question of which features are to be extracted from a pattern (signal) does not seem to have received serious consideration in the PR literature related to AE. And, in particular, the approaches adopted seem to be ad hoc or arbitrary and not based on any formal theory. Thus, the need for developing a guideline has motivated us to study the feature extraction problem from a theoretical perspective by modelling the pressure waves with some representative, typical and analytically tractable short-duration transient functions, and the transducer as a linear-phase bandpass system.

The feature extraction problem is studied using a large database of signals generated in accordance with the model developed and analysed. The four of the conventionally used time-domain parameters, *viz.*, ringdown count, event duration, rise time, and peak amplitude are analysed in depth in terms of the discriminating information they carry. The results demonstrate the significance and efficacy of three of these parameters as features for pattern recognition or pattern classification of AE signals. In addition, some new time-domain parameters (*e.g.*, negative peak amplitude) with potential use in complex AE applications are identified.

3. Relevance of unsupervised pattern recognition

The second major problem of a PR process is the choice of a suitable classification procedure. Classification schemes essentially are of two types: supervised and unsupervised[1]. Supervised procedures require an adequately large set of preclassified training samples. In several AE experiments, due to the lack of sufficient a priori problem knowledge, the use of supervised procedures is unfeasible or if feasible, prohibitively expensive. This makes unsupervised procedures desirable or more relevant. Thus, in this work, total emphasis is placed on unsupervised PR methods.

4. Efficient unsupervised pattern classification procedures

In practice, normally, unsupervised pattern classification problems are solved by clustering using appropriate algorithms. Clustering algorithms aim at detecting the subgroups in the data corresponding to the pattern classes. Though numerous clustering algorithms are available in PR literature[2], most of them are problem-specific. Besides, several of these algorithms, on account of their enormous computational requirements, are unsuitable for real-world problems involving large volumes of multidimensional data to be analysed in short periods of time. This has prompted us to develop clustering procedures devoid of these shortcomings.

First, we develop a fast iterative threshold-distance algorithm. The efficiency of this algorithm for well-separated clusters is established by rigorous theoretical analysis and by experimental demonstrations on two-dimensional artificial data. For any type of data, the algorithm can be used as a fast means of generating hypotheses about its category structure. We next develop a versatile two-stage classifier (clustering

procedure) combining the threshold-distance algorithm and a conventional nonhierarchical clustering scheme[2]. The efficiency and versatility of this procedure is demonstrated on a variety of artificial data. Using these data, we further investigate some methods of deciding the number of clusters inherent in the data.

5. Demonstration on simulated AE data

In conformity with our stated goal, we subject the pattern recognition procedures developed and investigated to tests using laboratory-simulated AE data. Also, several clustering experiments performed on these data establish the significance of some of the time-domain parameters as features for signal characterisation and classification. Further, using these data, the effect of data normalization on clustering results, *i.e.*, whether normalization positively affects classification accuracy is also studied.

6. Classification of experimental AE data

The first set of experimental data used to test the pattern recognition procedures developed consists of AE signals generated by three different failure modes, *viz.*, fiber breakage, delamination, and splitting in GFRP composites. The second data set consists of AE signals collected from tensile tests conducted on GFRP plastic strain insulators. The experiments performed on both the data sets clearly establish the practical value of the postulated procedures for AE signal analysis.

7. Conclusion

To summarise, this work is put forward as (1) an exploration of the possibilities for the adaptation of unsupervised pattern recognition techniques for solving practical AE signal analysis problems, and (2) a demonstration of the soundness of the approach and its utility.

References

1. DUDA, R. O AND HART, P. E *Pattern classification and scene analysis*, 1973, Wiley.
2. ANDERBERG, M. R. *Cluster analysis for applications*, 1973, Academic Press.

Thesis Abstract (Ph.D.)

High pressure and thermal studies of arsenic based chalcogenide glasses by S. S. K. Titus

Research supervisors: E. S. R. Gopal and S. Asokan
Department: Instrumentation and Services Unit

1. Introduction

Arsenic-based chalcogenide glasses are of great interest due to their application in dry photography, infrared optics, electrical and optical devices, etc. A study of the physical properties of these glasses is highly desirable. To identify the appropriate material for efficient technological application[1,2], in the present investigation, high-pressure electrical resistivity, thermal crystallization and switching behaviours of some arsenic-based glasses have been studied. These studies throw light on the structure, electrical properties and their compositional dependence of these samples.

2. Experimental

Bulk, semiconducting As_xTe_{100-x} ($25 \leq x \leq 65$), As_2X_3 (X=S,Se,Te) and $As_xTe_{100-x-y}Se_y$ ($30 \leq x \leq 50$; $10 \leq y \leq 25$) glasses were prepared by melt-quenching method. Electrical resistivity measurements were made on these glasses, as a function of pressure up to 8 GPa and temperature down to 77 K, using a Bridgman anvil system, developed in our laboratory. Thermal crystallization studies were carried out using a Stanton–Redcroft differential scanning calorimeter (DSC). The switching behaviour of these samples was studied using a home-built PC-based system.

3. Results and conclusions

The resistivity of As_xTe_{100-x} and $As_xTe_{100-x-y}Se_y$ glasses decreases continuously with pressure, reaching metallic values around 6 GPa pressures[3,4]. The conductivity activation energies of these glasses, estimated at different pressures, also show that these glasses undergo a continuous semiconductor to metal transition under pressure. The most interesting aspect of high-pressure response of these glasses is the subtle change in the resistivity behaviour at compositions corresponding to the mean coordination number $Z=2{\cdot}4$. Such an unusual change in the resistivity behaviour is elucidated in the light of chemical and percolation thresholds, occurring in chalcogenide glasses[5,6]. Figure 1 shows the variation of electrical resistivity of $As_{35}Te_{65}$ and $As_{45}Te_{55}$ glasses, representing $Z < 2{\cdot}4$ and $Z > 2{\cdot}4$ regions, respectively.

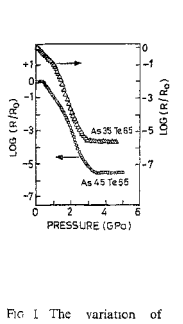

Fig 1. The variation of normalized electrical resistance of $As_{35}Te_{65}$ ($Z < 2{\cdot}4$) and $As_{45}Te_{55}$ ($Z > 2{\cdot}4$) glasses with pressure.

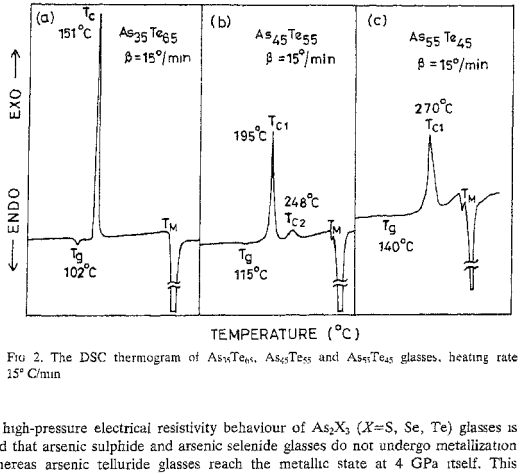

Fig 2. The DSC thermogram of $As_{35}Te_{65}$, $As_{45}Te_{55}$ and $As_{55}Te_{45}$ glasses, heating rate 15° C/min

A comparative study of high-pressure electrical resistivity behaviour of As_2X_3 (X=S, Se, Te) glasses is also undertaken. It is found that arsenic sulphide and arsenic selenide glasses do not undergo metallization up to 8 GPa pressure whereas arsenic telluride glasses reach the metallic state at 4 GPa itself. This observation indicates that in arsenic sulphide and arsenic selenide glasses with lower densities, the applied pressure is primarily taken for shrinking the voids rather than compressing the bonds[7].

Thermal crystallization studies on As_xTe_{100-x} glasses reveal that glasses with $x < 40$ and $x = 55$ and 60 exhibit a single glass transition and a single crystallization reaction (Fig. 2). However, glasses with $x = 40$, 45 and 50 show a double-stage crystallization (Fig. 2) The glasses are recovered after the first crystallization reaction and the intermediate phase is identified to have an fcc structure[8]. The activation energy of crystallization is estimated using Kissinger's method. It is found that a plot of composition *versus* crystallization temperature and the activation energy for crystallization also shows a slope change at a composition $x = 40$, corresponding to a mean coordination of $Z = 2{\cdot}4$[9].

The thermal behaviour of ternary As–Te–Se glasses shows very interesting results. These glasses with $Z = 2{\cdot}3$ (*i.e.*, $x = 30$, $10 \leqslant y \leqslant 25$) show a single glass transition and a single-stage crystallization. On the other hand, glasses with $Z = 2{\cdot}4$ and $Z = 2{\cdot}5$ ($x = 40$ and 50, $10 \leqslant y \leqslant 25$) show a single glass transition and a double-stage crystallization. The observed change over in the behaviour can be explained on the basis of chemical and percolation thresholds occurring in the systems.

The differential thermal and thermogravimetric analyses (DTA/TGA) on As_2X_3 glasses show that arsenic sulphide and arsenic selenide glasses do not show crystallization reaction on heating. Further, during

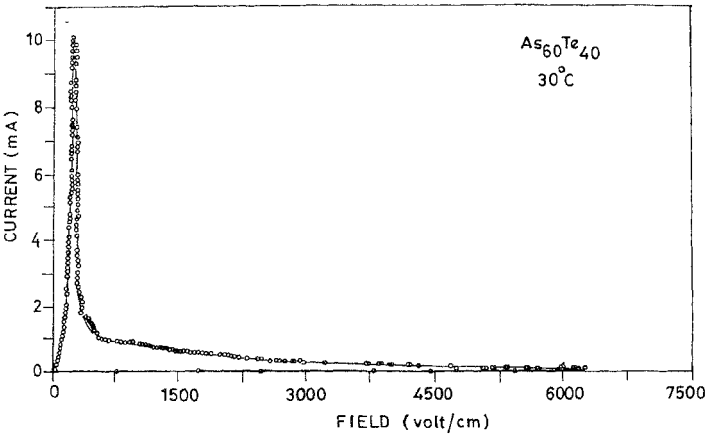

FIG 3. The I–V characteristics of $As_{60}Te_{40}$ glass at 30° C.

heating arsenic sulphide and arsenic selenide glasses show almost 100 and 50% weight loss, respectively, up to 825 K. About 20% weight loss is observed in the case of arsenic telluride glasses up to 825 K[7].

The I–V characteristics of $As_{60}Te_{40}$ and $As_{60}Te_{40}Se_{10}$, two representative glasses, are studied using a home-made PC-based system. These glasses, are found to exhibit switching with memory. Figure 3 illustrates the I–V characteristics of $As_{60}Te_{40}$ glass at ambient temperature. It is also found that the threshold voltages of these glasses decrease continuously with increasing temperature.

References

1. MOTT, N. F. AND DAVIS, E. A. — *Electronics processes in noncrystalline materials*, 1979, Clarendon.
2. ZALLEN, R. — *The physics of amorphous solids*, 1983, Wiley.
3. TITUS, S. S K., ASOKAN, S , RAMAKRISHNA, R. AND GOPAL, E. S. R. — High pressure studies on the electrical resistivity of As_xTe_{100-x} glasses, *Phil. Mag B*, 1990, **62**, 553–556.
4. TITUS, S. S K., ASOKAN, S. AND GOPAL, E. S. R. — High pressure room temperature and high pressure low temperature studies on As–Te–Se glasses, *J. High Pressure Res* , 1992, **10**, 629–635
5. PHILLIPS, J. C. — Vibrational threshold near critical average coordination in alloy network glasses, *Phys Rev. B*, 1985, **31**, 8157–8163.
6. PHILLIPS, J C. AND THORPE, M. F. — Constraint theory, vector percolation and glass formation, *Solid St. Commun.*, 1985, **53**, 699–702.
7. TITUS, S. S. K., ASOKAN, S , RAMAKRISHNA, R. AND GOPAL, E S. R — A study of high pressure behaviour of As_2X_3 glasses. In *Recent trends in high pressure research* (A.K. Singh, ed.), pp. 477–479, 1992, IBH–Oxford, New Delhi.
8. TITUS, S.S.K., ASOKAN, S., PANCHAPAGESAN, T.S. AND GOPAL, E.S.R. — Thermal crystallization behaviour of As–Te glasses, *Phy. Rev. B*, 1992, **46**, 14493–14500
9. TITUS, S. S. K., ASOKAN, S. AND GOPAL, E. S. R. — Compositional dependence of crystallization of As–Te glasses, *Solid St. Commun.*, 1992, **83**, 745–747.

Thesis Abstract (Ph.D.)

Studies on the reactivity of triphenylphosphine towards diruthenium(II, III) tetracarboxylates by Birinchi K. Das
Research supervisor: A. R. Chakravarty
Department: Inorganic and Physical Chemistry

1. Introduction

Dimetallic tetracarboxylates with an $M_2(\mu\text{–}O_2CR)_4$ core display strong bonding interactions between the metal atoms, particularly those of second- and third-row transition elements[1,2]. While the comparatively more stable forms of the tetracarboxylates of other transition elements are $M_2(O_2CR)_4$ and $M_2(O_2CR)_4L_2$ (L, a neutral or anionic monodentate ligand), for ruthenium it is the mixed-valent form $Ru_2(O_2CR)_4^+$, which is more stable. These diruthenium(II, III) tetracarboxylates are characterized by a unique spin-quartet ground state[1,2].

Tertiary phosphines (PR_3) react with $M_2(O_2CR)_4$ compounds to form either a biaxial or a biequatorial adduct[1,2] of formulation $M_2(O_2CR)_4(PR_3)_2$. Triarylphosphines also display[2] orthometallation reaction with the tetracarboxylates of Os and Rh. The diruthenum(II, III) tetracarboxylates by virtue of their unusual electronic structure show distinctly different reactivity patterns. Reactions of these complexes with tertiary phosphines are not thoroughly explored. Detailed investigations on these reactions constitute the subject matter of the present work.

2. Experimental

All synthetic work was carried out in solution medium. The complex $Ru_2Cl(O_2CMe)_4$ was prepared according to a reported[3] procedure. All products were obtained in solid state and were characterized by analytical, spectroscopic (electronic, IR, ^1H NMR, and ESR), magnetic, and electrochemical (cyclic and differential pulse voltammetric) data depending upon the applicability of the method concerned. Structural studies were carried out using single-crystal X-ray diffraction technique on representative compounds.

3. Results and discussion

To extend the scope of the present studies a series of diruthenium(II, III) tetraarylcarboxylato compounds of formulation $Ru_2Cl(O_2CR)_4$ (**1**) where R=C_6H_4–*p*–X, X = H(**a**), OMe(**b**), Me(**c**), Cl(**d**), and NO_2(**e**) has been synthesized by reacting $Ru_2Cl(O_2CMe)_4$ with RCO_2H. The room temperature μ_{eff} values for these paramagnetic precursor complexes (**1**) are found to correspond to the presence of three unpaired electrons per dimer. A quasireversible one-electron reduction process is observed at ~0.0 V (*vs* SCE) from cyclic voltammetric studies on the DMF solution of **1**. The crystal structure[4] of **1b** consists of the dimeric $Ru_2(\mu\text{–}O_2CC_6H_4\text{–}p\text{–}OMe)_4^+$ units bridged by chloride ligands into a polymeric zigzag chain where the average Ru–Cl distance and Ru–Cl–Ru angle are 2.567(2) Å and 121.0(1)°, respectively. The average Ru–Ru distance in **1b** is 2.286(1)Å.

The reaction of **1** with PPh_3 in an MeCN–H_2O medium leads to the formation of four series of products containing a (μ–aqua/oxo) bis(μ–carboxylato) diruthenium core. At low temperature a mixed-valence diruthenium(II, III) complex $Ru_2(\mu\text{–}OH_2)(\mu\text{–}O_2CR)_2(\eta^1\text{–}O_2CR)_2Cl(MeCN)(PPh_3)_2$ (**2a–d**) has been isolated. By adding some extra water to the reaction medium the diruthenium(II) complex $Ru_2(\mu\text{–}OH_2)(\mu\text{–}O_2CR)_2(\eta^1\text{–}O_2CR)_2(MeCN)_2(PPh_3)_2$ (**3a–e**) has been obtained as the main product. In the triply bridged complexes[5] (**2b** and **3e**), the bridging μ–OH_2 ligand is hydrogen bonded to the η^1-bonded carboxylato ligands. Structural results on **2b** provide evidence for the localization of the oxidation states in the diruthenium(II, III) complex (**2**).

Two diruthenium(III) complexes $Ru_2(\mu\text{–}O)(\mu\text{–}O_2CR)_2(\eta^2\text{–}O_2CR)_2(PPh_3)_2$ (**4a–d**) and $[Ru_2(\mu\text{–}O)(\mu\text{–}O_2CR)_2(MeCN)_4(PPh_3)_2](ClO_4)_2$(**5a–c**) have been prepared by reacting **1** with PPh_3 in MeCN. Molecular structure of **4b** and **5a** show[6] the presence of a (μ–oxo)bis(μ–carboxylato)diruthenium(III) core in **4** and **5**. While the Ru–Ru sepearations in **4b** and **5a** are ~3.2Å, the Ru–(μ–O)–Ru angles are ~120°. The complexes containing labile facial sites serve as structural models for hemerythrin and other biomolecules[7]. Complexes analogous to **4** and **5** have also been obtained using $Ru_2Cl(O_2CMe)_4$ as the precursor.

The spectroscopic, magnetic, and electrochemical properties of complexes **2–5** have been studied[5,6]. An intervalence transfer (IT) absorption band for the asymmetric mixed-valence complex (**2**) is observed in the range of 900–960 nm in $CHCl_3$. This band is characteristic of a moderately coupled Class II mixed-valence[8] complex. The one-electron paramagnetic complex (**2**) exhibits an axial ESR spectrum with $g_\parallel$ ~2·3 and $g_\perp$ ~1·7 in the X-band at room temperature. The spectrum is as expected for an isolated $S_{\frac{1}{2}}$-Ru(III) centre. At low temperature the spectrum becomes rhombic. The diamagnetic complexes **3–5** display well-resolved ^1H NMR spectra consistent with their formulations. The μ-OH_2 ligand in **3** is highly deshielded because of hydrogen-bonding interactions. The oxo-bridged complexes display strong visible charge transfer bands originating in the {Ru–O–Ru} moiety.

The aqua-bridged complexes **2** and **3** are redox active in CH_2Cl_2-0.1M TBAP. The Ru_2(II, III)/Ru_2(II, II) and Ru_2(II, III)/Ru_2(III, III) couples for both the complexes are nearly reversible. Observed $E_{1/2}$ values are found to be dependent on the substituents present in the carboxylato ligands. Complex **2** undergoes a novel disproportionation reaction in MeCN medium to give the diruthenium(II) and diruthenium(III) complexes **3** and **5**, respectively.

In the above products formation of an Ru–Ru bond is precluded due to large separation between the metal atoms. However, at elevated temperatures the reactions also lead to the formation of metal–metal bonded anionic complexes along with complex **4**, the major product. The following cationic–anionic complexes[9] have been isolated from the reaction mixture. $[RuCl(MeCN)_3(PPh_3)_2]_2[Ru_2Cl_2(O_2CC_6H_4\text{-}p\text{-}Me)_4]$ (**6**), $[RuCl(MeCN)_4(PPh_3)][Ru_2Cl_2(O_2CC_6H_4\text{-}p\text{-}Me)_4]$ (**7**), and $[RuCl(MeCN)_3(PPh_3)_2]_2[Ru_2Cl_2\ (O_2CR)_4]$ (R=Ph, **8**; C_6H_4-*p*-Me, **9**). In the diruthenium(II) $[Ru_2Cl_2(\mu\text{-}O_2CC_6H_4\text{-}p\text{-}Me)_4]^{2-}$ anion of species **6**, the metal–metal distance is 2.291(1)Å. The cationic complex found in **7** is different from those in the other complexes. The Ru–Ru bond distance in the anionic complex of **7** is 2.299(1)Å. Using

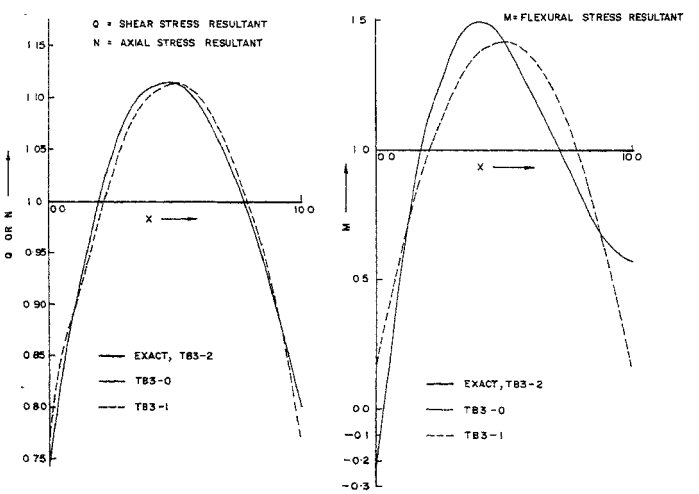

FIG. 1. Schematic representation of the pathways involved in the reaction studied. (i) PPh_3, MeCN, reflux; (ii) PPh_3, MeCN; (iii) PPh_3, MeCN–H_2O, 10° C; (iv) MeCN, reflux; (v) MeCN, RT; (vi) MeCN, RT; (vii) MeOH, NaO_2CR, RT; (viii) MeCN, $HClO_4$; (ix) MeCN, RT or reflux.

$Ru_2Cl(O_2CMe)_4$ as the precursor a product analogous to **8** and **9**, $[RuCl(MeCN)_3(PPh_3)_2]$ $[Ru_2Cl_2(O_2CMe)_4]$ (**10**) has been isolated, but in this case it is accompanied by a monomeric ruthenium(II) complex[10] $[Ru(O_2CMe)(MeCN)_2(PPh_3)_2]$ ClO_4 (**11**). Contrary to the other ruthenium(II) complexes present in the cationic–anionic complexes this complex (**10**) contains an acetato ligand in the chelating mode of coordination.

Magnetic susceptibilities of complexes **7–10** correspond to the presence of three unpaired electrons per molecule. These complexes display axial ESR spectra at 77 K in the solid state. Complex **6** is ESR silent and it contains only two unpaired electrons. While the data suggest a $\sigma^2\pi^4\delta^2(\delta^*\pi^*)^3$ configurtion for the anions of complexes **7–10**, the possible ground electronic configuration for the anion of **6** appears to be $\sigma^2\pi^4\delta^2\delta^{*2}\pi^{*2}$. This is apparent from the absence of a $\delta\rightarrow\delta^*$ transition band in **6**. The same transition for the complexes **7–10** is observed at ~1150 nm. All these paramagnetic cationic–anionic complexes display interesting ^1H NMR spectra in $CDCl_3$. The band assignments have been made on the basis of intensity ratios.

Mechanistic information has been extracted from structural and electrochemical data. The overall reaction involves both symmetric and asymmetric cleavage of the polymeric —Ru–Ru–Cl–Ru–Ru–Cl— chains present in the precursor complexes. Figure 1 shows the various possible pathways involved in the formation of the interesting range of products.

References

1. COTTON, F.A. AND WALTON, R.A. *Multiple bonds between metal atoms*, 1982, Wiley–Interscience.
2. COTTON, F A. AND WALTON, R A. *Struct Bonding* (Berlin), 1985, **62**, 1–49
3. MITCHELL, R.W., SPENCER, A. AND WILKINSON, G. *J Chem. Soc, Dalton Trans.*, 1973, 846–854.
4. DAS, B.K. AND CHAKRAVARTY, A.R. *Polyhedron*, 1988, **7**, 685–687; 1991, **10**, 491–494.
5. DAS, B.K. AND CHAKRAVARTY, A.R. *Inorg. Chem.*, 1990, **29**, 1783–1784; 1991, **30**, 4978–4986
6. DAS, B K. AND CHAKRAVARTY, A.R. *Inorg. Chem.*, 1990, **29**, 2078–2083
7. KURTZ, K.M. Jr *Chem. Rev.*, 1990, **90**, 585–606.
8. CREUTZ, C. *Prog. Inorg. Chem.*, 1983, **30**, 1–73.
9. DAS, B.K. AND CHAKRAVARTY, A.R. *Inorg. Chem.*, 1992, **31**, 1395–1400.
10. DAS, B.K. AND CHAKRAVARTY, A.R. *Indian J. Chem A*, 1992, **31**, 408–411

Thesis Abstract (M.Sc. (Engng))

Seasonal variation of the zonally symmetric tropical circulation in a simple climate model by Shankar Doraiswamy

Research supervisors: J. Srinivasan and Sulochana Gadgil
Department: Centre for Atmospheric Sciences

1. Introduction

A low-order model of the zonally symmetric tropical circulation is developed. The model extends the work of Davey and Gill[1] to include a realistic forcing, *viz.*, the solar insolation at the top of the atmosphere and surface-feedback effects.

2. The model

The model equations are linearized about a resting basic state and are solved on an equatorial β-plane. The vertical structure of the variables is separated by specifying a first baroclinic mode. The other modes are neglected since the latent heating due to cumulus convection forces mainly this mode in the tropics.

The time dependence of the variables is specified by a truncated Fourier series. This results in a system of coupled ordinary differential equations (ODEs) with latitude as the independent variable. A finite-difference technique is used to solve the two-point boundary-value problem.

The model circulation is forced by solar radiation. Moisture equation is decoupled from the system of equations by assuming saturation in the regions of ascent[1] (following Davey and Gill). Surface temperature perturbations and latent heating are determined interactively with circulation. Surface (ocean/land) processes are modelled by incorporating certain time constants which are functions of appropriate surface and atmospheric parameters (like mixed layer depth, Bowen ratio, etc.). These time constants reflect the timescales for heat transfer in the model domains, *viz.*, atmosphere, ocean and land.

3. Results of the numerical simulations

The results of two series of numerical experiments are discussed. The model planet is either an aqua-(all-ocean) or a terra-planet (all-land) in the first series while it has both ocean and land in the second.

The results of the numerical experiments with all-ocean and all-land surfaces show:

i) the effect of moisture on circulation. The presence of moisture is shown to result in a narrower zone of ascent and a stronger circulation.

ii) the effect of direct absorption of solar radiation by the atmosphere. It is shown that in the case of an atmosphere which is transparent to solar radiation, the tropical convergence zone (TCZ) tends to overlie the surface temperature maximum and the atmosphere is forced to respond on the same timescale as the underlying surface.

iii) the effect of different time constants for the ocean, land and atmosphere (the impact of various atmospheric and surface parameters which determine these time constants is discussed).

The results of the second series of numerical experiments show the effect of differential heating of the oceanic and continental surfaces. The location of the ocean–land boundary is varied in this series of experiments. Secondary maxima of surface temperature and vertical velocity are found in some cases. The results explain why a secondary TCZ is observed only in the Asian monsoon region and not over the African continent or the tropical Pacific and Atlantic Oceans.

Reference

1. Davey, M. K. and Gill, A. E. Experiments on tropical circulation with a simple moist model, *Q J R Met. Soc.*, 1987, **113**, 1237–1269.

Thesis Abstract (Ph.D.)

Intragenic pausing and regulation of CYP2B1/B2 genes in rat liver—role of heme by V. Venkateswar

Research supervisor: G. Padmanaban
Department: Biochemistry

1. Introduction

Cytochome P450 (CYP) genes form a superfamily and code for a variety of multifunctional monooxygenases that are involved in the metabolism of xenobiotics. Different chemicals induce distinct species of CYP genes[1]. Two prototype inducers are phenobarbitone (PB) and 3-methylcholanthrene (3-MC). 3-MC induces CYP1A1 and CYP1A2 genes in rat liver and is known to function through a steroid-hormone-like mechanism. The cytosolic Ah receptor moves into the nucleus upon binding of the ligand, binds to the *cis*-acting elements in the 5′ flanking region of the CYP1A1/A2 gene and activates transcription[2]. PB induces CYP2B1 and CYP2B2 genes. However, very little is known about the mechanism by which PB activates transcription of these genes.

Earlier work has shown that heme, in addition to the drug, is a positive modulator of CYP gene transcription[3–5]. Depletion of cellular heme results in the inhibition of drug-induced gene transcription. It has also been shown that binding of proteins to the 5′ near upstream region (–179 nt) of a CYP2B2 variant shows correlation to the transcription status of these genes[6].

The present study aims at elucidating the mechanism of regulation of CYP2B1/B2 gene in rat liver with special emphasis on the role of heme.

2. Materials and methods

Male rats of the IISc strain were injected with PB (8 mg/100 g, i.p.), $CoCl_2$ (6 mg/100 g, s.c.) or succinyl acetone (4 mg/100 g, i.p.) or combinations thereof. RNA preparations were analysed through dot blots, S1 nuclease protection or Northern blots. Transcription status of the genes was analysed using run-on transcription assays, using ^{32}P UTP. Hemin (10^{-6}M) or heparin (100 μg/ml) were added *in vitro* where relevant. Standard procedures were used[7]. Single-stranded DNA probes were generated by cloning suitable restriction fragments into M13 vectors.

3. Results and discussion

It was demonstrated that heme was a positive modulator of CYP2B1/B2 gene. Different chemicals that deplete cellular heme inhibited the drug-dependent gene activation to different extents. The ability of any chemical to inhibit CYP gene activation depends on the extent to which it can deplete cellular heme. A model was proposed to explain how different genes respond differently to cellular heme levels[8].

Studies with run-on transcription assay showed that heme regulates CYP2B1/B2 gene primarily at the level of elongation. The evidence was two fold: heme addition *in vitro* to heme-depleted nuclei could restore transcription to induced levels even under conditions where transcription initiation was blocked; and, heparin, which promotes elongation of nascent RNA chains *in vitro,* could overcome the effect of heme depletion.

Northern analysis of nuclear RNA, isolated from uninduced, induced and heme-depleted animals, indicated that heme could also act at the level of RNA processing and/or stability.

Further, it was also shown that intragenic pausing occurs in the CYP2B1/B2 gene and the effect of the drug might also be to relieve this pausing.

Use of single-stranded DNA probes led to the detection of significant amount of antisense transcription across the CYP2B1/B2 gene. The antisense transcripts were short molecules (around 200 nt) and could be detected in the nuclear RNA pool, though at very low levels. Interestingly, both antisense transcription and transcripts showed a heme-dependent inverse correlation to the sense transcription. However, a regulatory role for the antisense transcription can remain only speculative at this point.

4. Conclusions

This study has brought into focus elongation as a step in the regulation of CYP2B1/B2 gene transcription, especially with regard to the action of heme. Heme has also been shown to act at other sites including RNA processing and/or stability. An intriguing aspect of CYP2B1/B2 gene has been found in significant transcription occurring in the antisense orientation.

References

1 GONZALEZ, F. J. *Pharmac. Rev.*, 1989, **40**, 243–288.

2. YANAGIDA, A., SOGAWA, K., YASUMOTI, K-I. AND FUJII-KURIYAMA, Y. *Mol. Cell. Biol.*, 1990, **10**, 1470–1475.

3. RAVISHANKAR, H. AND PADMANABAN, G. *J. Biol. Chem.*, 1985, **260**, 1588–1592.

4 DWARAKI, V. J., FRANCIS, V. N. K., BHAT, G J. AND PADMANABAN, G. *J. Biol. Chem* , 1987, **262**, 16958–16962.

5. BHAT, G. J. AND PADMANABAN, G. *Arch. Biochem Biophys.*, 1988, **264**, 584–590.

6. RANGARAJAN, P. N. AND PADMANABAN, G. *Proc Natn Acad. Sci. USA*, 1989, **86**, 3963–3967.

7. AUSUBEL, F. M., BRENT, R., KINGSTON, R. E., MOORE, D. D., SEIDMAN, J. G., SMITH, J. A AND STRUHL, K. *Current protocols in molecular biology*, 1987, Wiley

8. VENKATESWAR, V. AND PADMANABAN, G. *Arch. Biochem. Biophys.*, 1991, **290**, 167–172.

Thesis Abstract (Ph.D.)

Digital simulation study of the application of artificial commutation in MTDC systems including weak ac networks by Premila Manohar

Research supervisor: H. S. Chandrasekharaiah
Department: High Voltage Engineering

1. Introduction

The technical advantages of HVDC transmission systems have paved the way for multiterminal HVDC (MTDC) systems. The MTDC systems with reduced losses, increased overload capabilities and well-coordinated control systems are operationally more flexible and secure than a number of point-to-point HVDC links. Contemporary MTDC system research is broadly concerned with control, load flow, stability and dynamic performance studies. MTDC systems interconnecting large ac systems invariably involve inversion into ac networks with low short-circuit ratio (SCR). This poses several special problems related to the reactive power compensation, voltage regulation and stability, dynamic overvoltages and commutation during abnormal conditions. The study of these problems is currently an active area of research. The present work is concerned with the dynamic digital simulation study of MTDC systems with reference to the problems of inversion into weak ac networks. The work contributes towards an understanding of the benefits which may be derived from using artificial commutation with series capacitors at inverters feeding weak ac network in MTDC systems. The protection of the series capacitors against overvoltages using metal oxide varistors is also investigated in detail.

Several measures have been proposed in literature to overcome the problems of inversion into weak ac networks. Significant among them include the use of synchronous condensers, static VAR system and/or sophisticated control techniques. Along with one of these techniques, the application of metal-oxide devices at the ac bus to limit dynamic overvoltages has also been considered in some cases. Notwithstanding the availability of these measures, the development of alternative remedial measures is still very relevant. In this context, the principle of artificial commutation using series capacitors emerges as a promising option. Although this method was mooted as early as 1921, its application in HVDC transmission systems has not yet been realized. The main reason for this has been, perhaps, the lack of suitable means to protect the series capacitor banks against overvoltages which invariably occur in these systems. However, with recent developments in metal-oxide varistor technology, it is of considerable interest to investigate the dynamic performance of artificially commutated inverter (ACI) with the series capacitors protected by means of ZnO varistor and the influence of this ACI on the performance of overall MTDC system. Of further interest, in the study of ACI, are the issues pertaining to dc harmonics and the evaluation of capacitor value. A systematic study of dc harmonics, the evaluation of capacitor value and the protection of series capacitors by ZnO varistor device is considered in this work. This study employs a newly developed digital simulation technique which has the merit of being simple and suitable for checking new concepts with reasonable accuracy and less computational efforts.

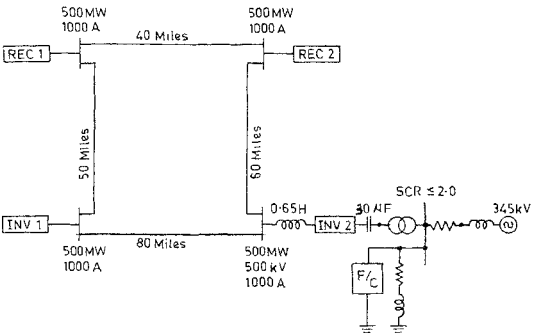

FIG. 1a. MTDC test system.

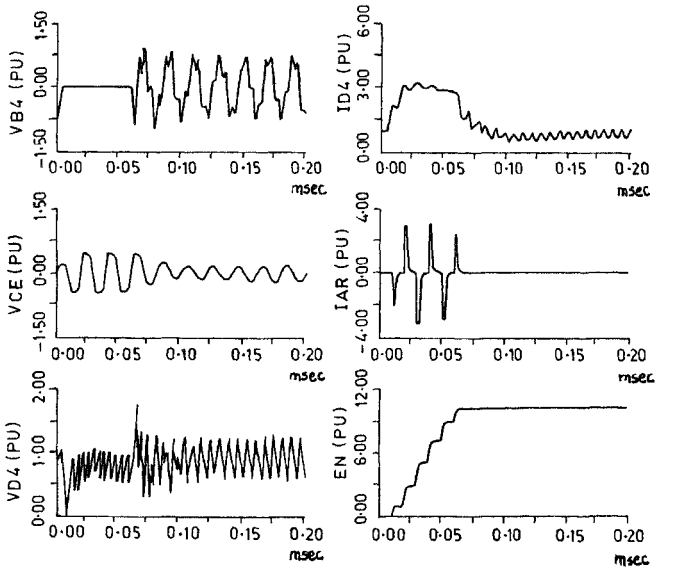

FIG 1b. Balanced ac fault at ACI, C-30μF.

2. Simulation technique

The digital simulation technique for the dynamic analysis of MTDC system is based on splitting the whole system into a number of subsystems and analysing them separately. For the purpose of illustration, a typical 4-terminal, mesh-connected MTDC system is considered (Fig. 1a). The converter model used in this analysis can incorporate natural and/or artificially commutated converters with equal ease. The numerical results are first obtained for the case of MTDC system with all the four converters connecting strong ac networks. This case forms the basis for further studies. To check the validity of the digital simulation technique and also to gain experience in using this algorithm, steady-state and few transient case studies have been carried out on this system. The equivalent ac system impedance is then varied at one of the inverter stations so as to make the ac system weak. Subsequently, the technique of artificial commutation is used at this inverter to overcome the problems of inversion into weak ac system.

3. Results and discussion

Before the analysis of MTDC system, including artificially commutated inverter (ACI), is taken up, the performance of a 12-pulse ACI with series capacitors is investigated. In particular, a semi-analytical procedure is outlined to determine an acceptable value of the capacitor required for stable operation. This analysis leads to an expression for the minimal value of the capacitor in terms of overlap angle. Although this procedure takes into account the strength of the connecting ac system and the steady-state characteristics, it fails to consider the effect of transients in the system. A parametric study which overcomes this limitation is further proposed.

The subsequent studies in this work are addressed to the dynamic performance of ACI in the MTDC system. Here the value of the capacitor which not only gives a satisfactory steady-state performance but also leads to an acceptable performance during severe transient cases is obtained based on a parametric study. The results of the analytical procedure developed earlier for the 12-pulse converter are used as guidelines in this study. The dynamic performance of ACI is shown to depend crucially on the value of the capacitor chosen. The capacitor value which results in admissible levels of valve stresses and dc harmonic content and a statisfactory performance during severe transient conditions is adjudged to be acceptable.

An important observation, however, is that, irrespective of the value of the capacitor considered, the series capacitors are invariably subjected to high overvoltages. This, perhaps, is the major shortcoming of the artificial commutation using series capacitors. This problem can, however, be eliminated if one resorts to providing protection against overvoltages. The problem of protection of the series capacitors is similar to that of protecting the series capacitors in EHV ac transmission lines. In the present study, it is proposed to use a protective device in the form of a nonlinear ZnO varistor across the capacitors. The energy rating of the varistor is determined from the worst case disturbance criterion. Here, a balanced ac ground fault for three ac cycles is considered to be the severe most disturbance. Figure 1b shows the numerical results for this case. For the system considered, this results in an energy absorption of 10.2 MJ. This value is feasible from the point of view of practical availability of the ZnO varistor. The numerical results obtained point towards the usefulness of artificial commutation for inversion into weak ac system and highlights the suitability of using varistor protection for the capacitors[1,2].

References

1. MANOHAR, P. AND CHANDRASEKHARAIAH, H. S. — Artificial commutation for inversion into weak ac system in a multiterminal HVDC system, *Electr. Power Sys. Res.*, 1990, 19, 95–104.

2. MANOHAR, P. AND CHANDRASEKHARAIAH, H. S. — Application of ZnO varistor protection to capacitors of artificially commutated inverter in MTDC system, Paper 90 WM 193-03 PWRS, 1990 *IEEE-PES Winter Meeting*, Atlanta, GA, USA, 1990.

Thesis Abstract (Ph.D.)

Algorithms and interfacing techniques for simulation of large scale power system dynamics by R. Sreerama Kumar
Research supervisors: H. P. Khincha and Lawrence Jenkins
Department: Electrical Engineering

1. Introduction

This work deals with the development of computationally efficient algorithms as well as interfacing techniques for both conventional transient stability analysis and real-time simulation of power system dynamics.

The transient stability analysis of a large interconnected power system involves the solution of a large set of differentio–algebraic system of equations. This requires considerable computation time. The development of algorithms and the modelling get further complicated by the presence of components such as static VAR-compensating systems, HVDC links, etc.

Due to increasing transfer of power among areas, both voltage limitations and transient stability limits are becoming the major source of restriction for secure pool operation. Thus, the incorporation of transient stability simulation function in a dispatcher training simulator is becoming increasingly important. However, in most of the dispatcher training simulators, the transient stability simulation has not been included because it cannot be done in real time using the state-of-the-art techniques.

2. Investigation of computation techniques

In real-time simulation, computation time is very important. In transient stability simulation, on the other hand, a marginal increase in computational costs can be tolerated to obtain the desired accuracy. Thus, the step size for numerical integration in real-time simulation is much higher than that considered in transient stability simulation. However, the increase in step size is accompanied by an increase in the number of iterations per time step for the solution of the network equations, and the risk of numerical instability. Ideally, it is desirable to arrive at a noniterative algorithm which can provide scope for a large step size without affecting numerical stability and solution accuracy. Hence, the search for computationally efficient, sufficiently accurate algorithms for simulation of power system dynamics continues.

In this work, first, some investigations are carried out to arrive at a unified algorithm for both transient stability and real-time simulation. Various algorithms are developed through different combinations of choices of synchronous machine model, numerical integration technique, method of interfacing the solutions of the algebraic and the differential equations, angle corrector formula, and convergence criteria for network solution. These algorithms are compared on the basis of computation speed and solution accuracy, and an appropriate combination is arrived at, for both transient stability analysis and real-time simulation. The simultaneous implicit method using trapezoidal rule appears to be the best for both transient stability and real-time simulation.

3. A high-speed algorithm for simulation of large-scale power system dynamics

A major part of the total computing time is consumed by the number of iterations per time step for the solution of the network equations. Thus, for improving the computational efficiency, it is desirable to minimize these iterations per time step. Therefore, various sources of network solution iterations are examined so as to investigate the possibility of reducing them. A two-tier approach, based on simultaneous implicit method[1], is proposed for the iterative solution of the set of algebraic equations of the network and the set of differential equations of the synchronous machines and the associated control systems. In this algorithm, at each time step, a real power (P)–rotor angle (δ) convergence is first obtained iteratively, with the terminal voltage being initially held constant at the value of the previous step. Once this coarse convergence is obtained the algorithm proceeds for final convergence with iterations using the triangularized admittance matrix. The significant point is that the network solutions, which are computationally intensive,

are avoided in getting the P–δ convergence. Further, the P–δ loop execution is quite fast, as it involves only multiplication/division–addition operations, and is confined to generator nodes only. A typical large Indian power system is used as the test system. The investigations reveal that the proposed algorithm, in general, shows significant improvement in efficiency over the algorithm built in production-grade programs.

4. Modifications for real-time applications

In transient stability simulation, the details of the disturbance to be simulated are known at the beginning of simulation. This is not so in real-time simulation, since, for instance, any circuit breaker can be opened or closed at any time by the system or plant operator, the instructor, and the plant logic.

Without changing the basic structure, the proposed algorithm has been made suitable for real-time simulation also, for operator training. This is implemented through certain simplifying assumptions and modifications. Simulation results are presented for these modifications also.

5. Transient stability simulation of unbalanced power systems

Conventional transient stability simulation is performed on the basis of a balanced system representation. However, a typical power system may be unbalanced due to a variety of reasons, and the computations of sequence quantities due to these unbalances are necessary to facilitate the application of countermeasures. An algorithm has been proposed for the simulation of power system dynamics under unbalanced operating conditions. The algorithm is a logical extension of the simultaneous implicit method, and makes use of the two-tier approach for the iterative solution of the algebraic and differential equations. As the network elements are represented in the phase frame of reference, the key step in the algorithm is the formation of the three-phase bus admittance matrix. Any change in the network configuration can be simulated merely by modifying this base-case admittance matrix. The algorithm is capable of simulating systems with time varying and random loads.

6. Practical applications

A few practical applications of the proposed algorithms considered are the dynamics simulation of systems which have induction motor loads and arc furnace loads. The methods of interfacing the induction motor model, with the proposed algorithms, is based on the prediction of flux linkages, implemented in electromagnetic transients program (EMTP)[2-4]. This technique is expected to provide a numerically robust algorithm. Induction motor dynamics during free acceleration, bus short circuit faults, and bus transfer are simulated. A computationally efficient method of modelling and interfacing of arc furnace loads with the algorithm for unbalanced transient stability simulation is also presented. The approach makes use of compensation theorem, and is similar to the method of interfacing time-varying elements with EMTP[5]. The proposed interfacing technique for the simulation of electric arc furnace load gives the solution with acceptable accuracy, in a minimal amount of time. The results of such applications are validated against earlier published results and/or by independent methods, and are found to match closely.

7. Conclusions

The modelling, interfacing and simulation techniques described in this work are applied to practical systems. The investigations reveal that the proposed algorithms can be uniformly applied for both transient stability analysis and real-time simulation of power system dynamics.

References

1. DOMMEL, H. W. AND SATO, N. Fast transient stability solutions, *IEEE Trans.*, 1972, **PAS-91**, 1643–1650.

2. BRABDWAJN, V. AND DOMMEL, H. W. Interfacing generator models with an electromagnetic transients program, Paper No. A76359-0, presented at the *IEEE PES Summer Meeting*, Portland, July 1976.

3. RAMANUJAM, R. A method of interfacing Olive's model of synchronous machine in an electromagnetic transients program, *EMTP Newsl.*, 1982, **3**, 46–59.

4 LAUW, H K — Interfacing for universal multimachine system modelling in an electromagnetic transients program, *IEEE Trans*, 1985, **PAS-104**, 2367–2373

5. DOMMEL, H.W — Nonlinear and time-varying elements in digital simulation of electromagnetic transients, *IEEE Trans.*, 1971, **PAS-90**, 2561–2567

Thesis Abstract (M.Sc. (Engng))

Inhomogeneous electric field breakdown study in pure SF_6 gas using ac and impulse voltages by B. S. Manjunath
Research supervisors: M. S. Naidu and M. C. Ratra (CPRI)
Department: High Voltage Engineering

1. Introduction

The application of gas-insulated systems (GIS) using SF_6 gas insulation in high-voltage electric power systems has been widespread on account of their various advantages, such as small size, high degree of reliability, etc. In view of this, a complete knowledge of all the aspects of the electric discharge properties of this gas has become essential. In spite of the various advantages, it has been well established that GIS are very sensitive to the presence of anomalies, such as a fault or the presence of particles which lead to the breakdown of internal insulation, either as soon as it is commissioned or later on due to switching or lightning surges. These particles act as sources of highly non-uniform electric fields, and cannot be eliminated or detected easily. Therefore, a better understanding of the breakdown phenomena is crucial to evaluate the role of discharges emanating from the particles and other sources of non-uniform fields in GIS. It is seen from the literature[1] that earlier studies have been carried out over a wide range of non-uniform fields, and gas pressures but at a single gap spacing, or over a range of gap spacings but at a single gas pressure, or over a range of gas pressures and gap spacings but only for a fixed rod diameter, and using only one or two types of applied voltages, but not over a wide range of field non-uniformities, gap spacings and gas pressures using different voltages simultaneously. The latter is essentially the aim of the present study in which a comprehensive study of electrical breakdown in SF_6 gas has been attempted for the first time. Investigations were carried out in compressed SF_6 gas under 50 Hz ac, lightning (1.2/50 μs) (LI), and switching (250/2500 μs) (SI), impulse voltages with rod-plane configurations of various rod diameters varying from a sharp needle (D≈0) to 12.0 mm, for different gap spacings of 5.0 to 100.0 mm, over the gas pressure range of 0.1 to 0.49 MPa.

2. Experimental apparatus and procedure

The experiments were carried out in a high-pressure chamber of approximately 200 l capacity, with an air–SF_6 condenser-graded cast epoxy bushing of 450 kV ac, 1050 kV impulse voltage rating fixed at the top of the chamber. The electrode is fixed inside the chamber through the window provided on the chamber. A moving seal with a counter to measure the gap distance is provided at the bottom of the chamber to move the bottom electrode. The chamber is capable of withstanding pressures up to 1.0 MPa. All electrodes used were made of brass. SF_6 gas used was 99.99% pure. A 100 kV ac transformer and 12-stage 2.4-MV, 30-kJ impulse voltage generator were used as voltage sources. Impulse voltages were measured using conventional step-by-step method. Where required, the up-and-down and Bekken's methods were also used[2]. All the experimental data could be reproduced to well within ±3%, and the spread in the average values was always within ±3%.

3. Results and discussion

3.1. *Effect of field non-uniformity on ac breakdown voltage*

Breakdown voltages are obtained in compressed SF_6 gas using 50 Hz ac voltage for different non-uniform field configurations, gas pressures and gap distances varying from 5 to 30 mm. The results have been

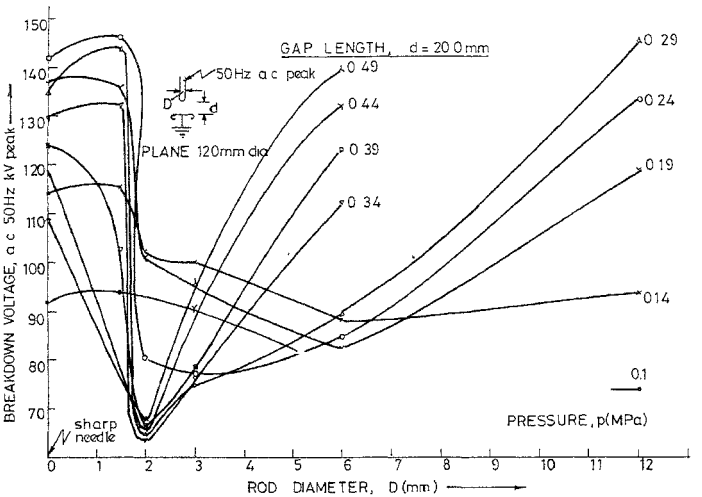

FIG. 1. AC breakdown voltage–rod dia characteristics for 20 mm gap length for different SF_6 gas pressures.

analysed and the variation of the breakdown voltages as a function of the degree of non-uniformity for different rod diameters is shown in Fig. 1. It could be seen from the figure that, for SF_6 gas, a safe voltage level exists below which no breakdown occurs irrespective of the field non-uniformity. The trend of flashover voltage to increase when the electrode becomes sharp could be interpreted to mean that for a given gap, irregularities on the electrode surface, such as sharp needles, protrusions, roughness, etc., do not necessarily diminish the insulation properties of the SF_6 gas. However, under these conditions, the presence of corona will deteriorate the insulation. Thus, such anamolies should be avoided. It is seen from the figure that the minimum breakdown voltage is 62.0 kV below which no breakdown could occur. If a higher operating voltage is chosen, say, for example, 70.0 kV, and a horizontal line is drawn at this level, then it will have two limiting points for each pressure. These two points, when plotted as a function of pressure (Fig. 2), will represent the upper and lower limits of a region within which breakdown will occur, and this is called the 'forbidden zone'. For values of radius of curvature outside this zone, no flashover will occur and may be considered as safe zone for operation. Figure 2 shows the forbidden zone for voltage levels of 70.0 and 125.0 kV of the present study and also of the work done by Azer and Comsa[3]. The upper boundary of the forbidden zone represents the safe limit for both corona and breakdown, and the pressure range of 0.25 to 0.35 MPa appears to be advantageous to use in a practical system.

3.2. *Lightning and switching impulse breakdown voltage characteristics*

Experiments have also been carried out under lightning and switching impulse voltages for the rod–plane configuration using the gas pressures of 0.1 to 0.49 MPa and the gap spacings of 10 to 100 mm for the rod diameters varying from sharp needle to 12.0 mm. A typical diagram of the breakdown voltage data as a function of gas pressure for different gap lengths for a sharp needle under both polarities using both lightning and switching impulse voltages is shown in Fig. 3.

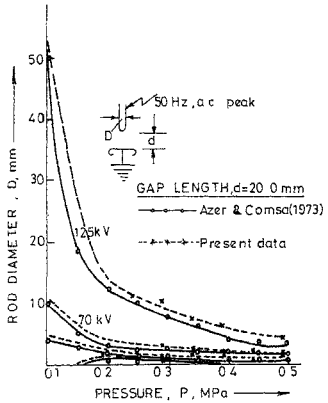

FIG 2 Forbidden zone for the rod diameter against pressure of a 20-mm rod–plane gap in SF_6 gas for operating voltages of 70.0 and 125.0 kV.

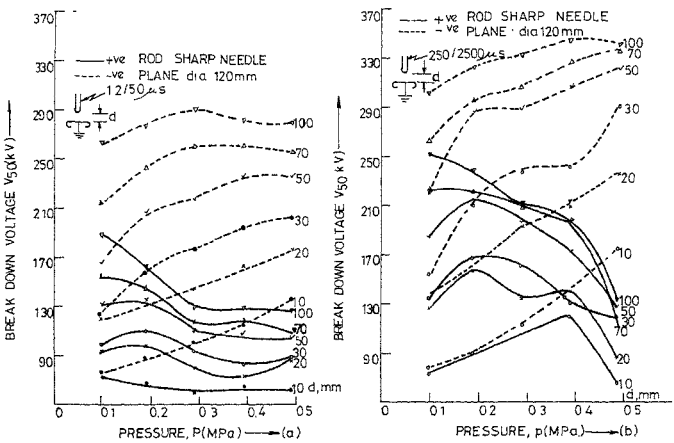

FIG. 3. Impulse breakdown voltage–pressure characteristics as a function of gap length for sharp needle (dia, D≈0)–plane configuration in pure SF_6 gas. (a) Lightning impulse and (b) Switching impulse.

From the experimental results it is seen that the SF_6 gas is sensitive to highly non-uniform fields under positive polarity lightning impulse voltages only and not under negative polarity voltages. Under highly non-uniform fields, the negative polarity switching impulse breakdown voltages are higher than the corresponding positive polarity values as in the case of lightning impulses; however, the magnitudes of breakdown voltage are higher under switching impulses than under lightning impulses.

It was also seen that the V_{50} values under positive polarity switching impulse are sensitive to highly non-uniform fields, and the negative polarity are sensitive only to moderately non-uniform fields. The 'forbidden zone' similar to the one shown in Fig. 2 under ac voltages has also been obtained for both under LI and SI voltages.

3.3. *Comparison of data under ac, LI and SI voltages*

The experimental data obtained under different voltages have been compared for gap lengths of 10, 20 and 50 mm for a sharp needle, and the results are shown in Fig. 4. It is seen from the figure that under highly non-uniform fields, under positive polarity, the impulse ratios are lower than one. This could be generally attributed to corona stabilization leading to the shielding of the point electrode[4].

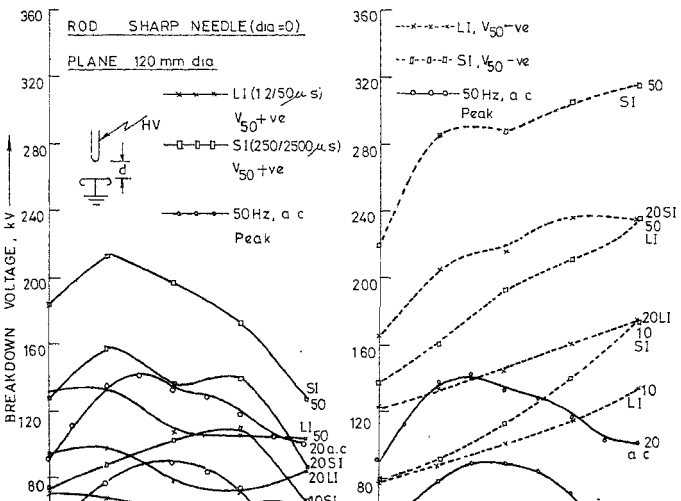

FIG. 4. Breakdown voltage–pressure characteristics for needle (dia ≃ 0 mm)–plane gap in pure SF_6 gas. (a) ac, positive polarity–LI and SI, (b) ac, negative polarity–LI and SI.

4. Conclusions

The breakdown voltages under slow rising voltages exhibit relatively higher values under highly non-uniform ficld suggesting that the surface roughness and the protrusions need not affect the insulation strength of the SF_6 gas, but the presence of corona due to these will deteriorate the gas purity and hence failure of insulation can occur. The breakdown voltages of the SF_6 gas are sensitive to highly non-uniform electric fields under positive polarity LI, and to moderately non-uniform electric fields under negative polarity SI voltages.

References

1 COOCKSON, A H	Review of high-voltage gas breakdown and insulators in compressed gas, *IEE Proc. A*, 1981, **128**, 303–312.
2 AZER, A A AND COMSA, R. P	Influence of field non-uniformity on the breakdown characteristics of sulfur hexafluoride, *IEEE Trans.*, 1973, **EI-8**, 136–142.
3. BEKKEN, H	Determination of characteristic voltages in impulse and switching surge testing, *IEEE Trans* , 1967, **PAS-86**, 962–968.
4. FARISH, O.	Corona-controlled breakdown in SF_6 and SF_6 mixtures, *16th Int. Conf. on Phenomenon on Ionised Gases*, Dusseldorf, 1983, pp 187–195.

Thesis Abstract (M.Sc. (Engng))

Evaluation of swirl chamber atomiser spray characteristic correlations by M. K. Venkataraman
Research supervisor: M. V. Narasimhan
Department: Mechanical Engineering

1. Introduction

In an effort to correlate the spray characteristics of swirl chamber atomisers with geometry and discharge pressure, several nondimensional characterizing functions have been proposed by a number of investigators[1]

The correlations proposed by Abramovich and Eisenklam reduce to an identical form when, n, the index of frictional decay in vortex motion, is equal to 1, *i.e.*, for free vortex conditions. Eisenklam's correlation reduces to that of Matsumoto and Takashima[2] when $n=0$. The correlation proposed by Doumas and Laster is similar to that of Eisenklam being its reciprocal with $n=0.5$. The correlation proposed by Giffen and Muraszew and Carlisle is similar and is based on free vortex flow.

Ranganadha Babu *et al*[3] have shown analytically that the correlating parameter proposed by Eisenklam, the air core coefficient and the index of frictional decay in vortex motion are related. The influence of geometry and discharge pressure on the thickness of the annular liquid film formed at the discharge orifice is examined analytically by Rizk and Lefebvre[4].

An attempt is made in the present study to examine the relative merits of the correlations, proposed by the earlier investigators, based on the data reported by Kutty[1].

2. Experimental test set-up

The test set-up was built around a Rolls Royce Derwent V aero gas turbine fuel system.

An air-trap was provided in the fuel line to separate air and allow foam-free liquid for the measurement of discharge. In the measuring bulbs the inflowing was directed against the wall to prevent foam formation.

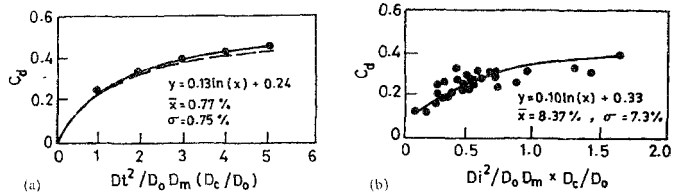

FIG. 1 Coefficient of discharge

Spray cone angle was measured by photographing the spray using the two-chamber method developed by Kutty. Air core diameter at the orifice was determined by photographing the axial view of the air core from the spray end. Orifice plane was illuminated through a perspex window provided at the rear of the atomiser.

Preliminary experiments were conducted with some atomisers fabricated by Kutty to determine discharge, cone angle and relative air core diameter. The results were compared with those of Kutty to examine the reliability of the results reported by him, as also the repetitivity of the results obtained from the test set-up. The agreement between the measured and reported results was within ±3%.

3. Evaluation of the correlations

A least square fit of the form $y = a\ln(x) + b$ was determined for the experimental data reported and correlating functions proposed by Eisenklam, Matsumoto & Takashima, Abramovich, Doumas & Laster, Giffen & Muraszew and Carlisle. A typical fit is shown in Fig. 1.

A comparison of the predicted results with each of these correlations for six nozzle configurations revealed that the variations in the predicted value of coefficient of discharge cone angle and relative air core diameter are 44.44, 34.8 and 12.65%, respectively, with respect to the maximum predicted value.

The above correlations are based on limited experimental data obtained at low discharge pressures. It was therefore considered that their comparison based on the extensive data reported by Kutty would be more meaningful.

Least-square logarithmic fits were determined with each of the correlating parameters using the data reported by Kutty (Fig. 2).

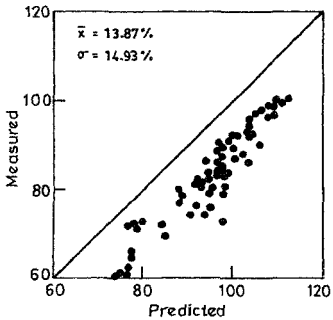

FIG. 2. Cone angle.

The maximum values of mean error and standard deviation for coefficient of discharge were 13.19 and 11.5%, respectively. Corresponding values for cone angle were even better, being 3.93 and 5.51%. The standard deviation and mean error for relative air core diameter were however uniformly high. The maximum and minimum values were 45.71, 27.63 and 34.37, 14.19%, respectively.

The spray characteristics computed from Ranganadha Babu and Lefebvre's analytical relations were compared with the experimental data of Kutty. It is observed that the predicted cone angle from Ranganadha Babu *et al*'s equations is generally higher than the measured values and that of Rizk and Lefebvre's consistently lower.

4. Conclusions

It is concluded that for predicting the coefficient of discharge and cone angle of swirl chamber atomisers the correlation of Matsumoto and Takashima appears to be the best. The maximum values of the precision parameters, mean error and standard deviation for the predicted coefficient of discharge and cone angles are 8.37, 7.3 and 4.15, 3.68%, respectively

Lefebvre's equations predict coefficient of discharge, cone angle and relative air core diameter of swirl chamber atomisers to within a precision of around 10%.

References

1. KUTTY, P. S. — *Some studies on the prediction of the performance characteristics and the design of swirl chamber atomisers*, Ph.D. Thesis, Deptt of Mechanical Engineering, Indian Institute of Science, Bangalore, India, 1974.
2. MATSUMOTO, S. AND TAKASHIMA, Y. — Design criteria of hollow cone nozzle and prediction of drop size distribution, *Proc First Int. Conf. on Liquid Atomisation and Spray Systems*, Tokyo, Japan, 1978, pp 79–85
3. RANGANADHA BABU, K., NARASIMHAN, M. V. AND NARAYANA SWAMY, K. — Design of swirl chamber atomisers, *Int J. Turbo Jet Engines*, 1987, **4**, 81–85.
4. RIZK, N. K. AND LEFEBVRE, A. H. — Prediction of velocity coefficient and spray cone angle for simplex swirl atomisers, *Int J Turbo Jet Engines*, 1987, **4**, 65–75

Thesis Abstract (Ph.D.)

Flow behaviour in a mixed flow pump with varying tip clearance by Timir Kanti Saha
Research supervisors: S. Soundranayagam and M. V. Narasimhan
Department: Mechanical Engineering

1. Introduction

The work describes an experimental investigation of the internal fluid dynamics of a mixed flow pump of specific speed $N_s = N\sqrt{Q}/H^{0.75} = 100$ rpm (metric) which corresponds to the range of specific speed of cooling water pumps in large power stations in India. The emphasis was on obtaining a detailed physical picture of the flow and understanding the underlying phenomenon thus helping to lay a foundation for rational design. The investigation was carried out on a special pump test facility that was designed and built for this purpose. A pump impeller was designed using the fundamental concepts of turbomachine theory and with a minimum of empiricism. Experimental measurements were used to verify the concepts implicit in the design methodology and also validate the computational techniques used to predict the internal velocity and angle distribution. The effects of scale were illustrated by comparing the pump performance with that of an identical machine being studied in a parallel investigation at low Reynolds numbers in an aerodynamic test rig. The work also included investigation of the effect of tip clearance on pump performance.

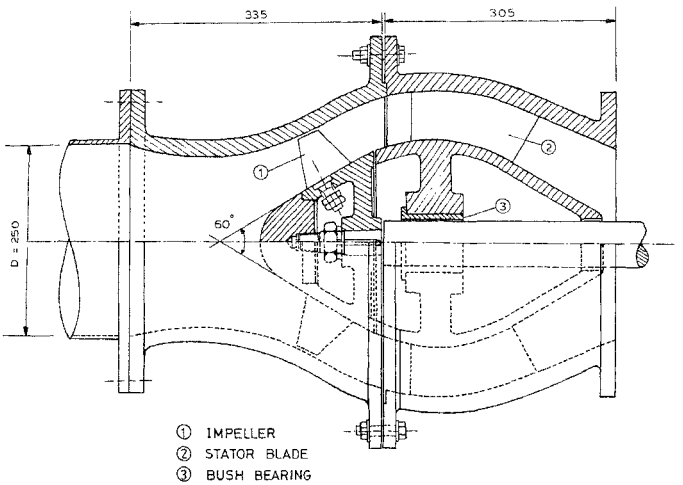

FIG. 1. Experimental impeller.

2. Experimental arrangements

The experiments were carried out in a closed-circuit test facility incorporating a resorber and having provision for the control of fluid temperature and pressure. The inlet tip diameter of the pump was 272 mm. Provision was made for detailed velocity and angle traverses immediately up and downstream of the impeller blades as well as downstream of the stator. All the three components of velocities were measured using multihole pressure differential probes. The overall flow rate was measured using a venturimeter calibrated *in situ*.

The test impeller is shown in Fig. 1. It has eight blades of aerofoil section, the blade shapes being obtained by conformal transformation of rectilinear cascades on to conical flow surfaces. The tip clearance could be closely controlled by axial adjustments of the impeller shaft.

3. Results and discussion

The measurements established that there was considerable three-dimensional flow with spanwise migration of the meridional stream lines specially at off-design conditions. Extensive recirculation occurred at the tip of the blades at inlet when the flow rate was severely throttled leading to pre-rotation of the incoming fluid. The decrease in flow rates also resulted in the presence of recirculating eddy at the hub at impeller exit. The change in the overall performance of the impeller at the onset of such recirculating eddies was too weak to be noticed in the head flow characterstic that continued to rise with reduction in flow rate without any sign of stall.

Figure 2 is a sample of the spanwise variation of meridional velocity at inlet to the impeller as the flow rate is decreased. The occurrence of flow reversal at the tip at reduced flow is clearly seen. This reverse

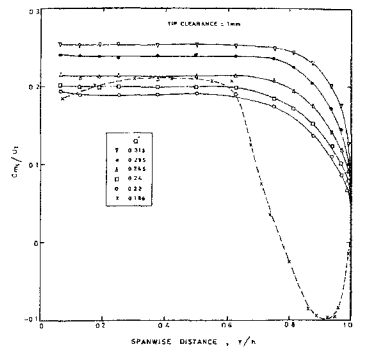

FIG. 2. Spanwise variation of meridional velocity at impeller inlet.

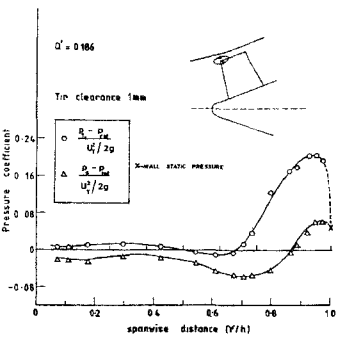

FIG 3 Spanwise variation of total and static pressure coefficient at impeller inlet

flow at the tip originates in the impeller blade spaces and hence carries angular momentum upstream in the reversal eddy. Turbulent mixing of the reversal eddy with the incoming flow transfers angular momentum to the latter causing it to rotate. The experiments established that such pre-rotation existed only when flow reversal at the tip was present. The repeated passage of the recirculating fluid in the tip reversal eddy through the blade space causes an increase in its total presseure due to repeated blade work (Fig. 3).

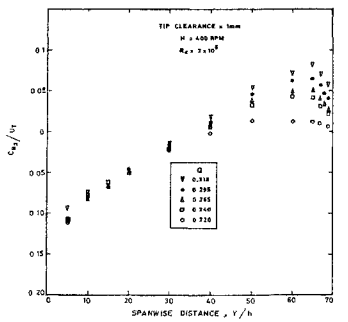

FIG. 4. Spanwise variation of tangential velocity at stator outlet.

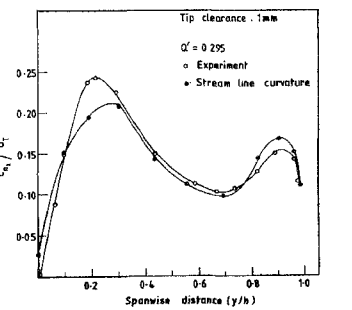

FIG 5. Variation predicted and experimental meridional velocity downstream of impeller.

It was possible from the experiments to separate out the work done by the Coriolis forces and aerofoil action. It was seen that aerofoil action is negative at the hub where Coriolis action predominates due to the large percentage change in flow radius. The results clearly indicate that, contrary to usual expectation, the use of 2D aerofoil data is at best a poor guide to the design of blading in mixed flow impellers.

Stator blades are provided in pumps to supposedly remove the swirl leaving the impeller. The experiments show that the stator blades can reduce the average swirl but cannot eliminate the interblade circulations associated with the streamwise vorticity carried over from the rotor. This is illustrated in Fig. 4 which shows the variation of tangential velocity downstream of the stator.

The present study strongly suggests that the complex flow in such mixed flow impeller can, for design purposes, be successfully predicted by modern computational techniques by assuming the flow to be axisymmetric. An example of the degree of agreement between the predicted and measured meridional velocity variation of the highly distorted impeller outlet flow is shown in Fig. 5. Results such as these can form the basis of rational pump design.

References

1. MYLES, D J. — *A design method for mixed flow fans and pumps*, Report No. 117, National Engineering Laboratory, 1965.
2. STIRLING, T. E. AND WILSON, G — A theoretically based CAD method for mixed flow pumps. *Eighth Tech. Conf. of the British Pump Manufacturers Association on 'Pump—The heart of the Matter'*, Cambridge, Paper No 15, pp. 185–203, 1983.
3. GUTON, P. — *Actual behaviour of pumps outside their high efficiency range (A tentative Survey), Lecture Series 1978–3*, Von Karman Institute for Fluid Mechanics, 1978.
4. CAREY, C., FRASER, S. M., SHAMSOLAHI, S. AND MCEWEN, D. — Flow analysis and part load performance of model mixed flow pump, *Int. Conf. on Part Load Pumping Operation, Control and Behaviour, Proc. Instn Mech. Engrs*, Paper No. C 339/88, pp. 83–88, 1988.
5. SOUNDRANAYAGAM, S. AND RAMARAJAN, V. — Off design performance of a mixed flow pump, *Int. Conf on Part Load Pumping Operation, Control and Behaviour*, Paper No. C 332/88, pp. 13–24, *Proc Instn Mech. Engrs*, UK, 1988

Thesis Abstract (M.Sc. (Engng))

Some studies on partial contact in pin joints by Ashis Kumar Maity
Research supervisor: T. S. Ramamurthy
Department: Aerospace Engineering

1. Introduction

Joints are essential elements in load transfer between structural components. They are introduced in large structural systems for a variety of essential functions. Common examples are mating different materials, connecting different simpler or smaller components and provision for occasional or periodic disassembly for packing, transport, inspection, servicing, etc. Joints allow ease and flexibility of construction, choice of desirable load-transfer process, flexibility in size, shape and interchangeability of components. But the joints are also locations of high-stress concentrations and consequently form potential source of failure.

Among different types of joints, pin joints are extensively used to connect the components of an assembly. Clearly, each pin–hole combination creates stress concentration and is a potential source of structural weakness. The problem has, therefore, for many years, attracted extensive analytical and experimental investigation. The pin joint has been a difficult problem for analysis for over a number of decades. The

difficulties arise mainly due to the following reasons: (i) complex nature of load transfer at joint locations, (ii) three-dimensional effects, (iii) behaviour of misfit pin, (iv) frictional stresses at pin–plate interface, (v) pin bending, etc. Due to severe complexity of the problem most of the analysis in literature is based on some simplified models. Most of the earlier attempts were mainly concentrated on the simple problems of a perforated plate (*i.e.*, plate with a hole). They studied the stress distribution in a perforated plate under various loading conditions. Later, a few studies attempted to analyze the linear behaviour of push fit problem. With the advent of computer and advanced numerical techniques, researchers are now able to solve different aspects of stress analysis in pin joints[1-3].

2. Problem definition

A thin isotropic sheet with a circular pin in a circular hole is considered for analysis. The hole and the pin diameters are taken as 2a and 2a(1+λ) where λ is the proportional interference of the pin–hole combination and decides the fits of the joint to be either interference (λ>0), or push (neat, snug) (λ=0) and clearance (λ<0). The cases of nonzero λ may be classified as misfits. In the case of misfit pins the pin–plate interface exhibits partial separation/contact under loads. The extent of the separation is a non-linear function of load magnitude and is generally not known a priori. This leads to a changing boundary value problem and introduces nonlinearity in stress and displacement distributions with respect to load.

In the separation region, we have $\sigma_r=0$ and $U>a\lambda$. In the contact region, we have $U=a\lambda$ and $\sigma_r<0$. Thus, on the complete interface, we must have either

$$U \geqslant a\lambda \quad \text{or} \quad U = a\lambda$$
$$\sigma_r = 0 \qquad\quad \sigma_r \leqslant 0.$$

The above inequalities can be expressed in a single equation form as

$$(U - a\lambda)\,\sigma_r = 0.$$

The above equation must satisfy at every point on the interface boundary at any stage of contact/separation configuration.

3. Method of analysis

We use biharmonic polar trigonometric series solutions of Michell for the elastic fields of the pin and the sheet. For the pin portion we consider the body force potential function (V_B) along with stress function (ϕ_p). These identically satisfy the governing differential equation and some of the boundary conditions. The remaining boundary conditions are approximately satisfied with the help of collocation technique.

3.1. *Lug loaded through an interference fit pin*

A lug is nothing but a two-dimensional finite plate with a pin. Depending on the supporting edge location with respect to the loading direction, one gets either a pull or push load situation (Fig.1). The difference in stress concentration factors for the two configurations is brought out clearly. This has an important bearing in estimating the fatigue crack growth studies of critical joints in the aircraft industry, thus influencing the life of component and life cycle cost of the equipment. To confirm the analytical findings of bubble separation[4] a set of experiments using photoelasticity were conducted. The experiments were carried over for both push and pull type of loads. The behaviour due to eccentricity of the pin position was checked, and initiation of separation was detected using a make-and-break of electrical circuit. The symmetry in the problem was exploited by locating the electrical circuit paths at 10° intervals but with 5° offset on the two sides of the axis. Thus, without cluttering up the specimen the experimental data for each 5° step were obtained (Fig. 2).

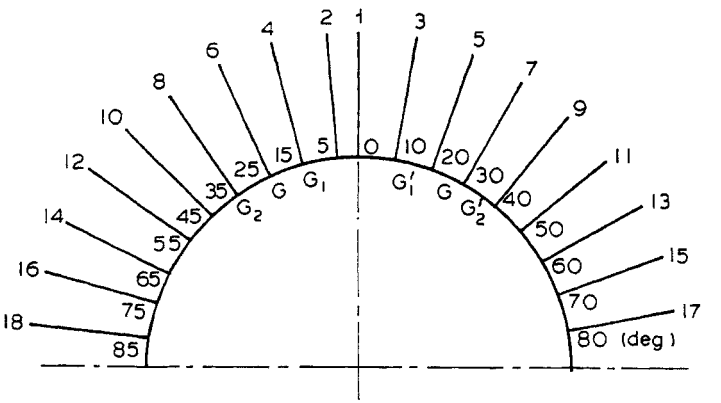

FIG 1.

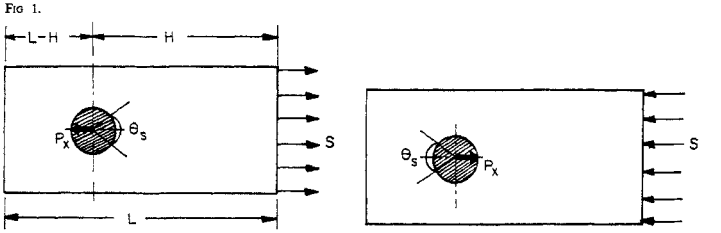

FIG. 2.

4. Important results

The results of continuum solutions using body force potentials have shown that the anamolies of earlier results especially for very soft pin are removed. This has resulted in the reduction of critical load parameter for onset of separation. Most of the results obtained by analysis are for ideally smooth interface between the pin and the hole surface. The change in the stress concentration factor between pull and push loads is small for radial stress as compared to hoop stress.

References

1. DE'JONG, T. Stresses around pin-loaded holes in elastically orthotropic or isotropic plates, *J. Composite Mater.*, 1977, **42**, 313–331.

2. GHOSH, S. P. *Analysis of joints with elastic pins*, Ph.D. Thesis, Deptt of Aerospace Engng, Indian Institute of Science, Bangalore, India, 1977.

3 MARGETSON, J AND MORLAND, L. W — Separation of smooth circular inclusion from elastic and visco-elastic plates subjected to uniaxial tension. *J Mech Phys. Solids*, 1970, **18**, 295–309.

4 RAMAMURTHY, T S — Recent studies on the behaviour of interference fit pins in composite plates, *Composite Struct.*, 1989, **13**, 81–99.

Thesis Abstract (Ph.D.)

Asperity interaction effects in elastic contact between nominally flat rough surfaces by N. Govinda Raju
Research supervisors: M. R. Raghavan, B. Dattaguru and M. V. Narasimhan
Department: Mechanical Engineering

1. Introduction

Surface roughness has profound influence on the tribological performance of metallic and non-metallic surfaces. In rough surfaces, the contact may be plastic or elastoplastic in the first few cycles of load; it is entirely elastic after a few cycles of loading. Thus, the elastic contact of rough surfaces is of great practical significance.

The number of contacts per unit length increases significantly with decrease in separation between the contacting surfaces. Hence, the average spacing between the contacts decreases with decrease in separation. None of the statistical models reported in literature take into account the effect of variation in the average spacing between the contacting asperities on the deformation characteristics of the contacting surfaces[1–6].

2. Present study

A statistical model which takes into account asperity interaction effects in elastic contact between nominally flat rough surfaces is presented. For purposes of studying the effect of decrease in the average spacing between the contacting asperities in a real surface with increase in deformation, model surfaces with uniformly spaced identical (a) wedge-shaped asperities with cylindrical tip, and (b) conical asperities with spherical tip are proposed. The effect of variation of spacing between the asperities on the deformation characteristics of the model surface when compressed by a rigid plane is studied with contact restricted to the curved tip region of the asperities using finite element method for contact problems developed in this work. Expressions in dimensionless form correlating the quantities like load, real area of contact and total compliance with deformation are developed for the asperities in the model surfaces with the curved tip depth factor, $\lambda = 0{\cdot}5$, 3 and 6 and spacing ratio B/B′ in the range $1{\cdot}4\times10^{-5}$ to 0·85. (Here B and B′ are the base width of the asperities and the spacing between the asperities, respectively).

For studying the elastic contact between a rigid plane and a nominally flat rough surface with (a) wedge-shaped asperities, and (b) conical asperities, it is assumed that, at any separation, all the contacting asperities are uniformly spaced. Differential equations are formulated to define, for an elemental change in separation, the elemental changes in the load, area of contact and total compliance of an asperity in a real surface in terms of the asperity profile parameters and the correlating expressions defining the deformation characteristics of the model surface at the specified spacing ratio. The differential equations are numerically integrated to determine the load, area of contact and total compliance of the surface. This formulation permits the use of appropriate probability distribution functions for the asperity profile parameters like peak/summit height, peak/summit radius, flank angle and curved tip depth factor. In the present study, the peak/summit radius and the curved tip depth factor are assumed to be constant for all the asperities while the distribution of peak/summit height is assumed to be Gaussian.

The finite element method for two-dimensional and axisymmetric contact problems with zero pressure at the contact boundary nodes, developed in this work, predicts both the load and the pressure distribution accurately, irrespective of whether the contact boundary node is a corner or a mid node.

3. Conclusions

The study on model surfaces with (a) wedge-shaped, and (b) conical asperities shows that:

(i) The spacing ratio, B/B′, has profound influence on the deformation characteristics of individual asperities.

(ii) The geometrical area of interference, *i.e.*, the ratio of the real area of contact to the geometrical area of contact increases significantly with B/B′; the effect of λ on this increase is insignificant.

(iii) The stiffness of individual asperities at any λ and $B/B' > 0{\cdot}05$ is inversely proportional to the flank angle of the asperity. At any flank angle and $B/B' < 0{\cdot}6$ the rate of decrease in stiffness with increase in B/B′ is higher, the lower the value of λ. However, the stiffness per unit nominal dimension of the model surface increases significantly with B/B′.

(iv) The mean pressure predicted by the finite element analysis for B/B′ in the range 0 to 0·85 is 6 to 25% higher than that by Hertz theory and this deviation is higher, the smaller the area of contact.

(v) The dimensionless maximum shear stress increases significantly with B/B′ and λ. At $B/B' > 0{\cdot}2$, the dimensionless maximum shear stress is considerably higher than the value predicted by Hertz theory.

The study of contact between a rigid plane and a real surface with (a) wedge-shaped and (b) conical asperities reveals that:

(i) For separation $d/\sigma < 6$ (d is the separation between the rigid plane and the reference plane of the real surface and σ is the standard deviation of the peak height distribution in the real surface) and $\lambda > 3$, the load, area of contact and mean pressure on an asperity are significantly higher when interaction effects are considered; these increases are higher the smaller the height of the asperity.

(ii) Asperity interaction effects on the deformation characteristics of real surfaces with conical asperities and with wedge-shaped asperities are significant at separation, d/σ less than 5 and 6, respectively.

(iii) The variation of total area of contact with total load is very nearly linear in the case of interaction also.

(iv) For any separation $d/\sigma < 6$, the total compliance of the real surface is considerably higher when interaction effects are considered.

(v) The stiffness of the real surface increases significantly with separation and approaches a constant value at a separation d/σ of about 4. For $\lambda > 3$, the stabilized value of the stiffness increases significantly with λ.

References

1. GREENWOOD, J. A. AND WILLIAMSON, J. B. P. — Contact of nominally flat rough surfaces, *Proc. R. Soc. Lond. A*, 1966, **295**, 300–319.

2. KRISHNAMURTHY, T — *Elastic analysis of contact between nominally flat rough surfaces using finite element method*, Ph.D. Thesis, Indian Institute of Science, Bangalore, India, 1986.

3. WEBSTER, M. N. AND SAYLES, R. S. — A numerical model for the elastic frictionless contact of real rough surfaces, *Trans. ASME*, 1986, **108**, 314–320.

4. WEST, M. A. AND SAYLES, R. S. — A 3-dimensional method of studying 3-body contact geometry and stress on real rough surface. Interface dynamics (D. Dawson, C.M. Taylor, M. Godet and D. Berthe, eds), *Proc. 14th Leeeds–Lyon Symp. on Tribology*, Lyon, France, 8–11 Sept. 1987, Elsevier, 1988, pp. 195–400.

5 BEERTHE, D. AND VERGNE, PH. — An elastic approach to rough contact with asperity interactions, *Wear*, 1987, **117**, 211–222.

6. ESWAR, V. A , DATTAGURU, B. AND RAO, A. K. — Partial loss of contact in interference fit pin joints, *J. Aeronaut. Soc. India*, 1979, **83**, 233–237.

Thesis Abstract (Ph.D.)

Biomechanical modelling of manual materials lifting operations — a study on Indian workmen by S. Dasgupta
Research supervisors: K. N. Krishnaswamy and T. Ganguly
Department: Management Studies

1. Introduction

Manual operations of lifting loads, that we encounter in industrial as well as agricultural sectors, may be analysed in three different approaches, namely, the physiological, the psycophysical and the biomechanical modelling approaches. Of these, the biomechanical approach is relatively new, and has the advantage of examining the operations in a much wider perspective with the help of the present-day computational facility. It has its limitations, of course, in investigating the repetitive operations where human fatigue plays a very important role.

This study aims at exploring the feasibility of using biomechanical modelling methods in evaluating occupational stress and predicting the maximum lifting capability of Indian workmen engaged in manual lifting operations.

For this purpose, a six-link sagittal plane static model (described in Fig. 1) for human body was developed to suit Indian workmen. The lengths of these links are derived from selected anthropometric dimensions using widely referred empirical relationships. The weight and location of the centre of gravity of each link were also derived from the body weight and link lengths in a similar way.

The stress distribution was analysed in terms of forces and torques on the low back (L5/S1) and the knee which are two most important joints involved in lifting operations.

An effort was made to determine the maximum lifting capability by comparing the analytically calculated torque at each joint with its maximum voluntary strength limit for the population obtained from published data.

It has been found in the past that some of the biomechanically best postures are unacceptable to workers in practice. One of the possible reasons may be the existence of correlations, among different body angles governing the body posture, that make some of the theoretical combinations invalid. Therefore, the study was also designed to examine the existence of correlations among body angles.

It is necessary to extend the domain of application of the biomechanical models directly or indirectly to repetitive tasks to make the models more effective in investigating real-life work situations. An effort has been made in this study to extend the application of the model to repetitive lifting task by finding the possibility of existence of any statistical relation between lifting capabilities at single and multiple frequencies of lifting.

2. Experiments and data collection

For the analysis of stress distribution on the low back (L5/S1) and the knee joints, anthropometric characteristics and body weight of 17 healthy male workers were measured as required by the model.

A program was written in PASCAL to calculate the stresses at the low back and the knee for all possible combinations of body angles which are feasible to keep the body with load in equilibrium. The program also finds out minimum average stress on the body for different load weights and load heights.

For the prediction of maximum lifting capability, the selected anthropometric dimensions required by the model and the body weights were recorded for 25 male workers. Moreover, each worker was asked to stand on a platform and pull a spring balance fitted to it. The pull of the balance simulated maximum lifting capability of the worker. The exact body posture was recorded by lateral photograph with a grid at the background. The workers were asked to repeat the experiment for another two levels of load height

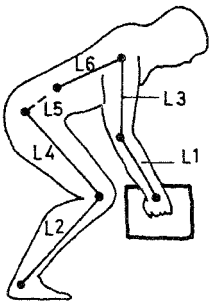

Relation between body dimensions and body links

Symbol	Body dimensions (cm)	Link lengths (cm)
D1	Stature	L1 = 1·0709 * D4 + D3
D2	Standing elbow height	
D3	Wrist to grip centre	L3 = 5·806 + 0·9646*D4
D4	Lower arm length	L4 = 13·2817 + 0·8172 * D5 D9 = 0·304 * D6 D10 = (D2 + L3) − (D9 + L2 + L4)
D5	Lower leg length	L5 = 0·195 * D10
D6	Foot length	L6 = 0·806 * D6

FIG. 1. Link representation of lifting posture

created by raising the worker's standing position with layers of bricks. A program was written in PASCAL to find out the maximum lifting capability by comparing the torque at each joint at the recorded posture with the maximum strength limit of the joint. The postural data collected in this experiment was also used to find the correlation among different body angles.

For finding out statistical relation between maximum lifting capabilities at single and multiple lifting frequencies, two groups of workers were selected. The workers were asked to pull the spring balance in free style with factory uniform excluding shoes. Each of the first group of 40 workers was asked to participate in three experimental sessions with lifting frequencies of 1 lift/min, 3 lifts/min and 6 lifts/min. A rest of 20 minutes was given between two sessions to eliminate the effect of fatigue. The peak heart rate was recorded before and after each session for each worker. In a similar way, the second group of 30 relatively healthier workers were asked to pull for frequencies of 1 lift/min, 6 lifts/min and 12 lifts/min.

3. Results and discussion

The study as a whole revealed some important facts and supported some existing concepts. The theoretical analysis of stress distribution (in terms of forces and torques) on the low back and the knee joints revealed that the knee and the back forces were inversely correlated and thus neither of them can be considered independently while optimizing the overall stress on the body in lifting activities. It was found in the analysis that workers bring the load closer to the body to minimize the overall force on the body during lifting.

It was found that bending the knee and straightening of the back as has been recommended by several past researchers, still serves as a useful rule in lifting.

In 76% of the cases, the model could predict the maximum lifting capability with significant ($p<0{\cdot}001$) correlation (close to 0·8) and regression coefficients.

Significantly high correlation coefficients were found between several body angles. The knee and ankle angles were always found to be inversely (negative) correlated for all levels of lifting heights and had a highest value of $-0{\cdot}744$ and significant at $p<0{\cdot}001$ level.

High correlation coefficients of the order of 0·8 and significant at $p<0{\cdot}001$ level were observed between maximum lifting capabilities at single and multiple lifting frequencies.

References

1. BEJJANI, F J , GROSS, C M. AND PUGH, J W — Model for static lifting. relationship of loads on spine and the knee, *J. Biomech.*, 1984, **24**, 281–286.
2. CHAFFIN, D. B. — A computerized biomechanical model—development of and use in studying gross body action, *J. Biomech.*, 1969, **2**, 429–441.
3 GARG, A. AND CHAFFIN, D. B. — A biomechanical computerized simulation of human strength, *AIIE Trans.*, March 1975, 1–15
4 DUTTA, S. P AND KULKARNI, V. P. — Biomechanical investigations on postural attitude and strength capabilities of Indian workers, *J Instn Engrs (India)*, 1981–1982, **62**, *IDGE* (1–2), 4–10.

Thesis Abstract (Ph.D.)

Consistency and correctness principles in quadratic displacement type finite elements

by B. P. Naganarayana
Research supervisors: B. Dattaguru, T. S. Ramamurthy and G. Prathap
Department: Aerospace Engineering

1. Introduction

Locking and stress oscillations have been serious problems confronting researchers in the field of finite element formulation of constrained media elasticity. Many heuristic explanations and techniques have been offered in the literature, but with partial success. The present work is directed at pinning down the exact reasons for these problems in displacement-type formulations and to eliminate them in an effective manner on a rational basis.

2. Fundamental principles

Now, it has been well known that the conventional isoparametric finite element formulation of constrained elastic media leads to some spurious constraints apart from the expected true constraints in the penalty limits[1]. The reasons for locking can be pinned down to these spurious constraints on a rational basis through a priori analytical error models for several simple elements[2]. The paradigm—*field-consistency*—thus evolved suggests the elimination of inconsistent terms in the strain energy expression that are associated with these spurious constraints for alleviating the problems of locking and delayed convergence.

The required reconstitution of the constrained strain fields cannot be done arbitrarily. The reconstituted strain field $\bar{\epsilon}$ and the conjugate stress field $\bar{\sigma}$ derived from it ($\bar{\sigma}=D\bar{\epsilon}$, where D is the rigidity coefficient) should satisfy an orthogonality condition

$$\int_\Omega \delta\, \bar{\sigma}^T(\bar{\epsilon} - \epsilon)\, d\Omega = 0 \qquad (1)$$

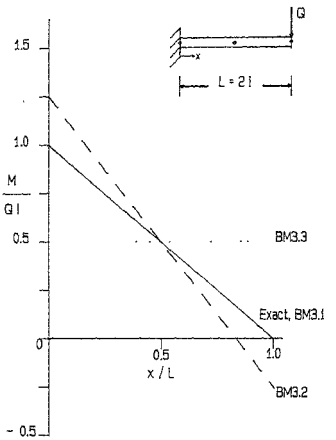

FIG 1. One element cantilever beam under tip shear force Q. Bending moment variation (BM3).

where ϵ is the strain field that is kinematically derived from the displacement fields. Equation (1) is derived from an equivalence of the minimum total potential energy (MTPE) principle with reference to the modified Hellinger–Reissner (HR) principle. Violation of such a requirement—*variational correctness*—induces spurious load mechanisms resulting in extraneous stress oscillations and non-existence of the Barlow points (Fig. 1). Due to the orthogonal nature of the Legendre polynomials in the domain of Gaussian quadrature, the method of expanding the inconsistent fields in terms of Legendre polynomials becomes a very simple efficient tool for consistency analysis (the term associated with the inconsistent Legendre terms directly gives the spurious constraint associated with it) and field reconstitution (just drop the inconsistent Legendre term).

It is recently observed that extraneous stress oscillations persist even when the formulation is field-consistent if the stress–strain relationship is non-uniform over the element domain (*e.g.*, tapered elements). In such cases, the stress (or stress resultant) fields are interpolated to a higher order when compared to the corresponding strain fields in an isoparametric displacement-type finite element formulation. Again, due to the orthogonal nature of the Legendre polynomials in the domain of Gaussian quadrature, these higher order Legendre terms do not participate in the strain energy computation and hence in displacement recovery. Thus, the nodal displacements recovered cannot identify these terms and result in oscillations of corresponding order if the stresses are computed from the strain fields directly using the constitutive relationships. Again, an equivalence of the MTPE principle with reference to the Hu–Washizu (HW) principle is sought to get the two orthogonality conditions required to reconstitute the strain and stress fields simultaneously:

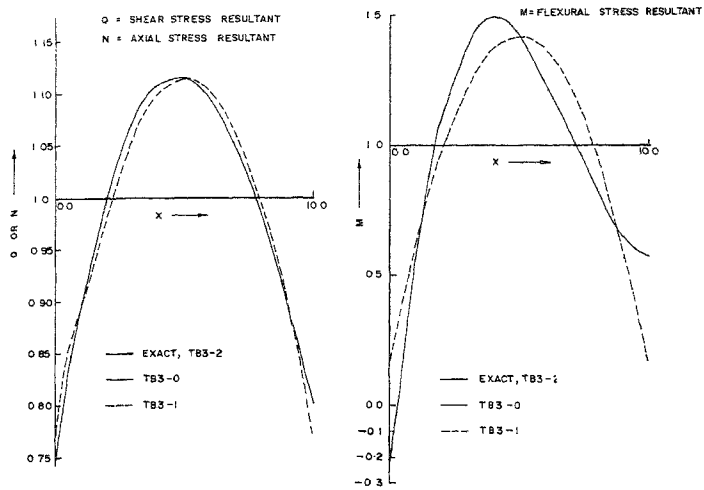

FIG 2. Quadratically tapered beam ($A_0 = 0.5$)–stress oscillations.

$$\int_\Omega \delta \bar{\epsilon}^T (D\bar{\epsilon} - \bar{S}) \, d\Omega = 0$$
$$\int_\Omega d \bar{S}^T (\bar{\epsilon} - \epsilon) \, d\Omega = 0. \tag{2}$$

The force and moment resultants from a tapered curved beam element[3] are plotted in Fig. 2 conforming to the above observations.

It is interesting to observe the modified consistency requirements when the mapping of the strain fields from the natural covariant system to the Cartesian system in an isoparametric formulations is non-uniform over the element domain. In such cases, the constrained strain field in the Cartesian system is interpolated to a higher order when compared to its order in the natural system. Thus, the order and the nature of the true and spurious constraints get modified in such formulations. For example, if the mid-node of a 3-noded Timoshenko beam element of length L is displaced from its central position by an amount Δ, the spurious constraints become

$$8 \Delta \theta_{,\zeta} + L \theta_{,\zeta\zeta} \to 0 \text{ and } \Delta \theta_{,\zeta\zeta} \to 0 \tag{3}$$

associated with the quadratic and cubic inconsistent Legendre polynomials in the constrained transverse shear strain field as against $\theta_{,\zeta\zeta} \to 0$ associated with the inconsistent quadratic term in the case of undistorted element. Thus, a distorted element may lock and show higher order stress oscillations while its undistorted counterpart does not lock!

There are several approaches to achieve consistency in the Cartesian system:

(i) *Cartesian base formulations:* Here the constrained fields are explicitly expanded in the Cartesian system and the inconsistent Legendre terms are dropped. This is the most effective method

(ii) *Covariant base formulation:* It is not always possible to expand the strain fields in the Cartesian system. In such cases, consistency can be achieved in the covariant natural system and then *consistently mapped* into the Cartesian system. This method is found to be very convenient in the plate/shell elements. But the generality of the method is limited in application since there is no state-of-the-art tool for consistent mapping which can be universally relied upon.

(iii) *Reduced integration:* This is the simplest to code and optimal integration strategies are possible for most of the elements. It should be noted that this often violates variational correctness, offers poor accuracy when the elements are distorted and not convenient in formulating composite elements.

3. Conclusions

The consistency and correctness principles discussed above form the basic guidelines for formulating finite elements that are free of locking and stress oscillations. The consistency and correctness requirements are analyzed and achieved for several quadratic displacement-type finite elements of practical interest. Finally, the relevance of these consistency and correctness principles is discussed with reference to finite element formulations in several other fields. The limitation of the work—non-availability of a universally applicable state-of-the-art tool for consistent non-uniform mapping—is mentioned.

References

1. PRATHAP, G. AND BHASHYAM, G. R — Reduced integration and shear-flexible beam element, *Int J Numer Meth Engng*, 1982, **18**, 195-210.

2 PRATHAP, G. — Field-consistency – Toward a science of constrained multi-strain-field finite element formulations, *Sadhana*, 1986, **9**, 345-353

3. NAGANARAYANA, B. P., PRATHAP, G., DATTAGURU, B. AND RAMAMURTHY, T. — Consistent force resultant distributions in a quadratic C–O beam element with varying sectional properties, *Int Conf. on Adv in Structural Testing, Analysis and Design, ICSTAD*, Bangalore, 1990

Thesis Abstract (M.Sc. (Engng))

Effect of landing platforms and exit closure on the drag force near the top portions of tall stacks by K. Suresh Kumar

Research supervisor: G. N. V. Rao
Department: Aerospace Engineering

1. Introduction

The static and dynamic effects of atmospheric wind on tall structures like satellite launch vehicles before lift-off, tall stacks of thermal and nuclear power stations, etc., have attracted considerable attention of research workers during the past three decades. It has been recently discovered that the loading over the top one to three diameters of stacks is considerably more than that elsewhere, although one would normally expect less load due to 'relief' of flow at the top[1,2]. This increase of coefficient of drag, C_D over the top portion of a stack has been incorporated in the latest ACI chimney code[3]. The present study is part of a programme directed towards better understanding of wind loading over the top portion of a stack. In this work, detailed experimental investigations of enhanced loading near the top of stacks with and without closing the mouth and with landing platforms of various sizes at different positions from the top have been made. The results, while confirming the higher loading, also suggest certain simple ways of alleviating this enchanced load by choosing the position and size of landing platforms.

2. Experimental results

Three models of tall stacks of model height between 1·10 and 1·25 m and different tapers were provided with static pressure holes at 90° in azimuth at different levels below the top to about five diameters below the top, along the four generators. The holes along a generator were unequally distributed, with a larger concentration near the top. There were altogether 48 holes in each model. Tests in a uniform wind at a Reynolds number of about 10^5 were conducted and pressures at every 10° in azimuth were measured by rotating the model. The pressures were integrated to get the drag coefficient. Tests were made with and without landing platforms. Photographs of surface flow patterns were taken using lampblack suspended in kerosene.

Tests confirmed the drag increase near the top in the absence of any platform. The effect of closing the mouth did not affect this conclusion. Small platforms at the top tended to increase the drag but, surprisingly, a platform at the top with an outer diameter equal to three times the stack diameter at the top completely nullified the enhanced along-wind loading. It was further observed that a smaller platform at about 1·3 times the outer diameter at the top, but located at 3 to 4 diameters below the top, also has the same effect of nullifying the enhanced along-wind loading.

3. Results and conclusions

A study of the pressure distribution and surface flow pattern indicated that the enhanced loading is due to higher suction associated with flow separation over the top. This higher suction penetrates to regions in the rear of the body thereby increasing the net along-wind load, although the positive pressure on the front is reduced near the top due to relief. This explains the observation that the along-wind load increases from zero at the top (in the absence of platforms) to a maximum value at about 0·5 diameters below, which is higher than the average value and slowly settles down to a nearly constant value below about 5 diameters. The landing platform near the top creates a higher pressure region on the front both above and below it by preventing the tendency of the flow to move towards the top and constraining it to move normal to the surface of the stack. The communication of this higher pressure to the rear regions reduces the suction which is more than the increased positive pressure at the front. These reasons have been suggested to explain the reduced along-wind load due to landing platforms.

Vickery's expression[4] for the along-wind load which is spread over several publications and contains several ambiguities has been rederived in a coherent manner.

References

1. OKOMOTO, T. AND YAGITA, M. — The experimental investigation on the flow past a circular cylinder of finite length placed normal to the plane surface in a uniform stream, *Bull. JSME*, 1973, **16** (No. 95), 805–814.
2. *ESDU-70014*, Engineering Science Data Unit, London, 1970.
3. *Standard practice for the design and construction of cast-in-place reinforced concrete chimneys*, ACI Standard, ACI 307-88.
4. VICKERY, B. J. AND BASU, R. I. — Simplified approaches to the evaluation of the across-wind response of chimneys, *J. Wind Engng Ind. Aerodyn.*, 1983, **14**, 153–166.

Thesis Abstract (Ph.D.)

Numerical study of some compressible boundary layer flows by Amalendu Sau
Research supervisor: G. Nath
Department : Mathematics

1. Introduction

During the last two decades a rapid growth of interest in the compressible boundary layer flows has accompanied developments in high-speed flight, jet engines, rockets, ballistics, combustion, gas turbines, ram jets and other novel propulsion mechanisms, heat transfer at high speeds and blast wave phenomena. Compressibility adds the obvious complication of varying density and also the effect of temperature variation on viscosity, since temperature variations tend to be wide in such problems. There are certain other features of boundary layer in a compressible flow. In compressible flow the boundary layers (including wakes and jets) are not the only regions in which viscosity and heat conduction effects are important, since these effects are also important in the interior and, in some cases, behind the shock waves.

2. Present study

This work is devoted to numerical studies of some steady and unsteady compressible boundary layer flows. The first problem deals with the semi-similar solutions for the problem of unsteady laminar compressible boundary layer flow at the most wind-ward generators of sharp cones on the plane of symmetry at the angles of attack with large injection rates. The influences of Mach number, total enthalpy at the wall, dissipation and cross-flow parameters on the flow and heat transfer have been discussed in detail. Steady nonsimilar solution for the problem with small injection rates has been studied by Libby[1]. In the second problem, the unsteady nonsimilar, compressible boundary layer flow over a rotating sphere has been investigated for various sets of values of parameters for rotation, mass transfer, Mach number and wall enthalpy. Solutions are obtained at different times, starting from the origin of streamwise coordinates to the point where streamwise skin friction reduces to zero. The unsteadiness in the flow field (for both first and second problems) is due to the free stream velocity which varies arbitrarily with time. In the third problem, we present the unsteady, compressible laminar boundary layer flow at the stagnation line of an infinite swept cylinder. A forced convection thermal boundary layer is produced by giving impulsive changes to the free stream velocity and to the wall enthalpy causing unsteadiness in the flow field. The effects of temperature parameter, fluid properties and transpiration cooling on the skin friction and heat transfer are considered. The fourth problem considers the steady nonsimilar laminar compressible boundary layer flow over an up and downstream moving wall with an applied magnetic field. The effect of variable gas properties and vectored mass transfer has been included in the analysis. Self-similar solution for the problem without magnetic field and gas properties has been discussed by Inger and Swean[2].

3. Results and discussion

The governing partial differential equations for each problem have been solved numerically by using quasilinearization technique in combination with an implicit finite difference scheme as developed by Inouye and Tate[3]. The effects of various parameters on skin friction, heat-transfer coefficients, velocity and enthalpy profiles for the above problems have been discussed in detail with the aid of graphs and tables.

From the results of the first problem it is observed that for small mass transfer (injection), the variation of density–viscosity product across the boundary layer, wall enthalpy, cross-flow and dissipation parameters have significant effect on the friction and heat-transfer coefficients. The velocity overshoot occurs and it is strongly dependent on the blowing rates, wall enthalpy and the dissipation parameter. For large blowing rates, the normal structure of the boundary layer is present, *i.e.*, a relative thick inner layer of constant properties and a relative thin outer layer adjusting the inner and external flows. The location of dividing stream line moves away from the surface as injection increases, but the effects are opposite as wall temperature and time increase. In the unsteady nonsimilar flow over a rotating sphere, the results show that skin friction and heat transfer respond to the unsteadiness in the external flow. Rotation and suction increase the skin friction and heat transfer for small values of streamwise coordinates but injection causes the opposite effect. In the subsonic range, the effect of Mach number is more pronounced on the heat transfer. Rotation, injection and a hot wall advances the point of occurrences of zero meridional skin friction towards the equator, whereas suction and cold wall delay it. In the unsteady boundary layer flow over a cylinder, it is observed that in the case where unsteadiness caused by giving an impulsive change to the wall enthalpy, it takes comparatively less time to reach steady state and the skin friction and

heat-transfer coefficients show much change immediately after receiving the impulse. But, in the other two cases, where unsteadiness is caused by giving an impulsive change to the free stream velocity, it takes comparatively more time to reach the steady state. The temperature parameter shows more effect on the heat-transfer coefficient than on the skin-friction coefficient and both of them decrease rapidly with injection. In the case of steady nonsimilar flow over an up and downstream moving wall in the presence of an applied magnetic field, it is observed that both skin friction and heat-transfer coefficients respond significantly on the variations of magnetic and dissipation parameters and on the viscosity index. As the magnetic and dissipation parameters increase, both skin friction and heat-transfer coefficients increase, whereas the viscosity index parameter shows the reverse effect. Velocity overshoot occurs which increases with the increase of magnetic parameter.

References

1. LIBBY, P. A. — Three-dimensional boundary layer flow with uniform mass transfer, *Phys. Fluids*, 1969, **12**, 408–417
2. INGER, G. R AND SWEAN, T. F — Vectored injection into laminar boundary layers with heat transfer, *AIAA J*, 1975, **13**, 616–622.
3. INOUYE, K. AND TATE, A — Finite difference version of quasilinearization applied to boundary layer equations, *AIAA J.*, 1974, **12**, 558–560.
4. LIU, T. M. AND CHIU, H H. — First and stable numerical method for boundary layer flow with massive blowing, *AIAA J.*, 1976, **14**, 114–116

Thesis Abstract (Ph.D.)

Modelling of liquid drainage and cell separation in foams by M. Venkata Ramani

Research supervisors: R. Kumar and K. S. Gandhi
Department: Chemical Engineering

1. Introduction

Cellular foam is a gas-in-liquid dispersion having a very high gas content (normally > 85%). It provides high interfacial area and low liquid hold up. These specific properties of foam make it suitable for effective separation of surface-active substances. Most of the biological materials are surface-active and can be separated by foam fractionation[1–3]. Some microbial cells too are surface active and have a tendency to get concentrated at the gas–liquid interface without addition of any external surface-active agents. Thus, foam offers an easy means of separation of surface-active cells from dilute broths.

2. Mechanism of foam drainage and cell separation

As foam is formed and moves up, it drains its liquid downwards due to gravity, thus reducing the liquid content of foam. The cells attached to the gas–liquid interface are unaffected by drainage, and hence the concentration of cells in the foam increases during its upward movement. The drainage thus has a profound effect on the final extent of separation and it is necessary to know the amounts of liquid drained to analyse the performance of any foam column as a separation device The present investigation is an attempt to develop from basic principles a model to predict the amounts of liquid drained.

The significant difference between the foams of cell broth and surfactant solutions is in the structure of films. Agglomerates of cells adhere to the interface. Thus the film is not flat on the liquid side. The adsorbed cells protrude into the bulk of the liquid and, because of their finite dimensions, reduce the amounts of liquid drained. In the present investigation, the drainage with both cells and surfactants was studied in batch as well as co-current foam columns.

3. Model for static foam drainage and cell separation

Static foams are batch and unsteady in nature. Hence they have the advantage of having higher amounts of drainage and lower final liquid hold up. A survey of the literature revealed that, though the subject has received much attention, only a few models are available for drainage in batch foams based on mechanistic considerations. In the present work, a model has been developed for drainage from surfactant solutions and cell broth, which predicts the liquid hold up, and hence the amounts of liquid drained, as a function of time. The foam is modelled as being made up of pentagonal dodecahedrons. It has essentially two components, namely, films and Plateau borders (junction of three films). The Plateau borders are further classified as horizontal or vertical depending on the angle they make with the vertical. The basic structural parameters and the expressions for film thinning and velocity through the Plateau borders were adopted from the available literature[4,5]. Material balance for all the three components of foam yielded three simultaneous first-order partial differential equations. The solution of these unsteady material balance equations requires formulation of some new boundary conditions. A few realistic assumptions made in the present investigation simplify the equations for films and horizontal Plateau borders to ordinary differential equations, which could be solved analytically. The equation for vertical Plateau borders however remains a first-order partial differential equation, and was solved by the method of characteristics[6]. Thus, the individual hold ups were obtained, and used for calculation of the amounts drained. The theoretically computed amounts of drainage were compared with those measured experimentally for a wide range of parameters. The agreement was found to be quite satisfactory.

Static foam drainage of microbial cells was then studied to account for the difference caused by the presence of cells. Experiments were carried out with *Saccharomyces carlsbergensis* which was selected for detailed investigation as it is known to exhibit high surface activity. The cells were grown for 18 h and separated from their broth by passing nitrogen through the broth. The separation factor, α, is defined as the ratio of concentration of cells in the foam to that in the residue. This was experimentally measured by analysing the concentrations of foam and residue. Modelling of drainage required incorporation of new ideas. The material balance equations remain the same despite the cells and it is the drainage mechanism that is altered by their presence. Of all the three components of foam, films are the most affected in this regard because of their smaller thickness. The film walls become corrugated due to the presence of cells and thus change the flow field in the film. An expression for the modified drainage of films was developed. The expression depends on the fraction of the area of films covered by the cell agglomerates. Further, when the film thickness reduces to the dimension of one cell agglomerate, the mechanism of drainage undergoes another change. Similarly, flow through the Plateau borders will also be modified when their triangular cross-sections reduce to accommodate just one cell agglomerate. Under such conditions, a new mechanism of drainage was proposed whereby films and Plateau borders are squeezed such that the cell agglomerate blocking the flow is swept out. It was proposed that during this stage the drainage rate is proportional to the liquid hold up. The drainage of films and Plateau borders thus follow different equations depending on the mechanism of drainage. These modifications were introduced into the material balance equations. They were solved to obtain the amounts of liquid drained as a function of time. From these, the separation factors could be theoretically predicted. The experimentally measured separation factors were compared with those obtained theoretically and the agreement was found to be quite satisfactory.

4. Exit foamate rates

The next step was the study of exit foamate rates and separation factors from vertical co-current foam columns. Exit foamate rate is defined as the rate of the liquid leaving the column at the top[7]. Experiments to find the exit foamate rates are different from those of static foams in that the foam is continuously generated and collected through an outlet. It was observed that foam moves vertically up until it reaches the base of the outlet port. As it moves further up, the direction of movement becomes horizontal. During this stage, the gravity-controlled vertical drainage still continues. Hence, the analysis of this section has to take into account the drainage while the foam moves horizontally. A model has been developed wherein the foam column has been idealized to be made up of two zones. The first zone extends from the foam–liquid interface to the base of the outlet port. Here the motion is entirely vertical. The second zone corresponds to the outlet zone. Here the motion is assumed to be entirely horizontal, but allowance is

made to account for the variation in the residence times of the elements of foam as they pass through the outlet zone. The basic mechanisms of film thinning and Plateau border drainage remain the same as for static foam drainage. Submodels for both the zones were developed which enabled the calculation of hold up in all the three components of foam. The simplified equations of the first zone were numerically solved with the boundary conditions defined. The equations for films and horizontal Plateau borders of the second zone were solved analytically whereas the equation for the vertical Plateau borders (a first-order partial differential equation) was solved by the method of characteristics. An expression for predicting the exit foamate rates was developed. The same framework was used to find exit foamate rates with cell agglomerates. For cell agglomerates, the modified film drainage and new mechanisms of drainage, after the critical conditions were reached, were, however, incorporated. The theoretically computed exit formate rates were compared with those obtained experimentally. The agreement found was quite satisfactory.

5. Conclusions

It can be concluded that models for static foams as well as dynamic foams were developed from first principles. The models successfully predicted the amounts drained and the exit foamate rates for surfactants and for cell agglomerates. While some models exist for surfactant solutions, this is perhaps the first model for cell agglomerates for both static and dynamic foams.

References

1 GRIEVES, R. B. AND WANG, S. L. Foam separation of *Pseudomonas gluorescens* and *Bacillus subtilis* var niger, *Appl Microbiol* , 1966, **15**, 76–81.

2. GRIEVES, R. B AND WANG, S. L. Foam separation of bacteria with a cationic surfactant, *Biotechnol. Bioengng*, 1967, **9**, 187–194

3 PARTHASARATHY, S., DAS, T. R AND KUMAR, R. Foam separation of microbial cells, *Biotechnol. Bioengng*, 1988, **32**, 174–183.

4. DESAI, D. AND KUMAR, R Flow through a Plateau border of cellular foam, *Chem. Engng Sci.*, 1982, **37**, 1361–1370.

5. DESAI, D. AND KUMAR, R Liquid holdup in semi-batch cellular foams, *Chem Engng Sci.*, 1983, **38**, 1525–1534.

6. ARIS, R AND AMUNDSON, N. R. *Mathematical methods in chemical engineering*, 1973, Prentice-Hall.

7. DESAI, D. AND KUMAR, R. Liquid overflow from vertical co-current foam columns, *Chem. Engng Sci.*, 1984, **39**, 1559–1570.

Thesis Abstract (Ph.D.)

Microstructural evolution during ordering and magnetic properties of rapidly solidified Fe–Si alloys by K. Raviprasad

Research supervisor: K. Chattopadhyay
Department: Metallurgy

1. Introduction

The Fe–Si system exhibits higher order structural ordering transitions as well as magnetic transition. The intersection of these higher order transition lines among themselves or with a two-phase field results in a critical point. However, understanding of the critical points in this system and their influence on the microstructural evolution remained unsatisfactory.

The aim of the present work is to fill this gap and to study the microstructural evolution in the Fe–Si system with emphasis on the role of critical points.

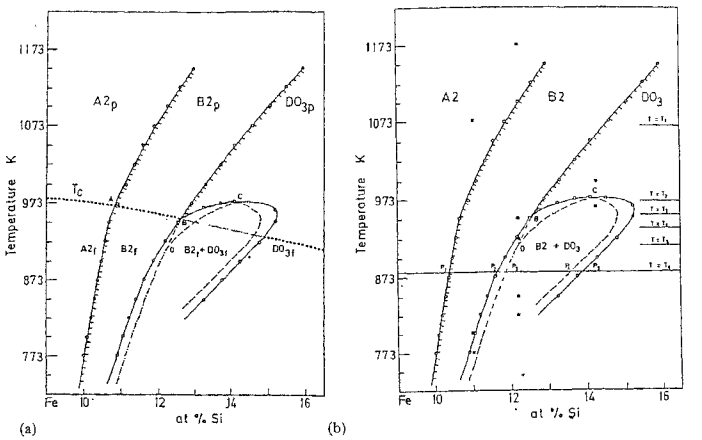

FIG 1. Partial-phase diagram of the Fe–Si system showing the different possible critical points with and without magnetic interactions (Fig. 1a and b, respectively). A: Tetracritical point, B: Bicritical point (1a) or Critical end point (1b), C: Consolute point and D: Metastable tricritical point.

2. Experimental

Alloys with silicon ranging from 8.7 to 14.2 at.% were prepared by three different rapid solidification routes (planar flow casting, meltspinning and twin rolling). The alloys were homogenised in single-phase field and isothermally treated within the B2+DO_3 two-phase field to study the microstructural evolution. Saturation magnetisation studies were carried out on these samples.

3. Results and discussion

Figures 1a and b show the phase diagrams of Fe–Si system with and without magnetic transition. The different possible critical points under these two conditions are marked. It is clearly seen that the bicritical point becomes a critical end point when we neglect the magnetic transition. The metastable extension of the higher order transition line in the two-phase field is marked by dashed line. Figure 2 shows the free energy composition diagrams corresponding to the temperatures (T_1–T_8) marked in Fig. 1b. The temperatures at which the samples are actually heat-treated are also denoted in Fig. 1b corresponding to the alloy composition studied. The free energy composition diagrams indicate that there is a possibility of conditional spinodal in this system if the higher order transformation precedes the first-order transformation. Earlier studies on Fe–Al system by Allen and Cahn[1] have shown that such a possibility exists. The results of microstructural evolution in the heat-treated samples show that the bright field as well as fundamental dark field micrographs are characterised by modulations. The modulations are found to be along 100 direction. Based on our analysis following the methodology of Laughlin *et al*[2], these were attributed to the spinodal decomposition. Figure 3a shows a bright field micrograph which clearly exhibits the modulations. Figure 3b shows a superlattice dark field image taken with a reflection common to both B2 and DO_3. The contrast within the B2-type domains, which was earlier referred to as anomalous contrast by Saburi and Nenno[3], is attributed to the renucleation of B2 along the APBs. The contribution to the superlattice reflection from the two phases differs as it depends on the volume fraction (depends on the phase boundary composition) and the order parameter of the two phases which are different and hence

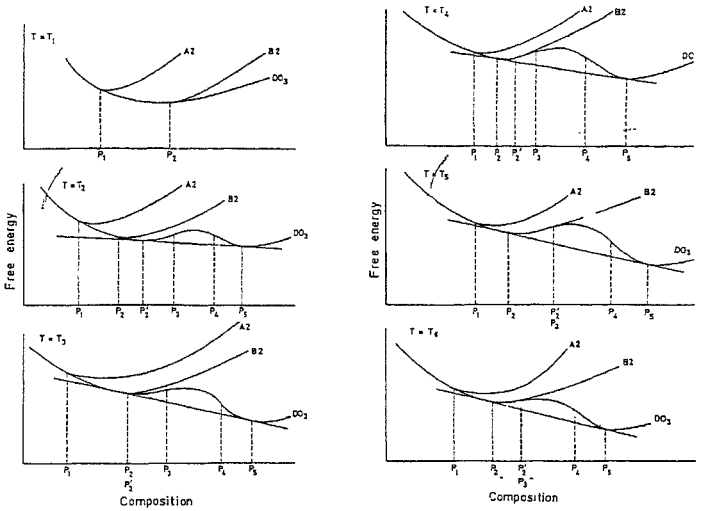

FIG 2 Free-energy composition diagram showing the possibility of conditional spinodal in the Fe–Si system The slope and curvature are continuous at the higher order transition point

FIG 3a Bright field micrograph showing modulations in heat-treated Fe–12 at.%Si alloy (948 K/12h–823 K/12h).

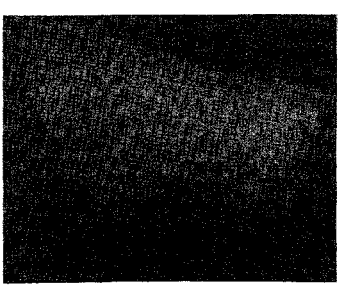

FIG. 3b Superlattice dark field from the same region shown in Fig. 3a.

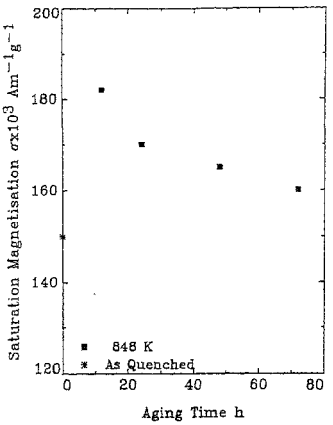

FIG 4 Variation of saturation magnetisation with isothermal treatment in Fe–12 at %Si alloy qualitatively reflecting the change in orderd structures.

the observed contrast. As the DO_3 spots are observed even in the samples heat-treated for the shortest duration within the two-phase field, the sequence of transformation in Fe–12.2 at.%Si can be summarized as

$$A2 \rightarrow B2 \rightarrow DO_3 \rightarrow DO_3' + DO_3'' \rightarrow B2 + DO_3.$$

A critical test for the proposed sequence has been provided by the measurement of saturation magnetisation as DO_3 structure with more of Fe–Fe bonds compared to B2 is expected to have higher magnetic moment. Figure 4 qualitatively reflects the proposed sequence. Thus, the initial rise in saturation magnetisation can be attributed to the formation of DO_3 and the consequent decrease is due to the renucleation of B2.

The effect of different rapid solidification processing on the ordering transformation and the microstructural evolution has also been studied. The B2 domain sizes were found to correlate with cooling rate in Fe–12 at.%Si alloy processed by different techniques. The observed magnetic properties were correlated with the structure.

4. Conclusions

1. Higher order transitions precede the first-order transition.
2. There exists a conditional spinodal in the Fe–Si system.
3. The B2 domain sizes were found to correlate with the cooling rate in Fe–12 at.%Si alloy.

References

1. ALLEN, S. M. AND CAHN, J. W *Acta Metall.*, 1976, **24**, 425–437

2 LAUGHLIN, D E , SINCLAIR, R AND TANNER, L E. *Scr Metall*, 1980, **14**. 373–376

3 SABURI, T. AND NENNO, S *Phil Mag*, 1967, **15**, 813–824.

Thesis Abstract (Ph.D.)

Some aspects of deformation and fracture in low cycle fatigue of a nimonic PE-16 superalloy by M. Valsan
Research supervisors: D. H. Sastry and S. L. Mannan
Department: Metallurgy

1. Introduction

Nimonic PE-16 is a nickel–iron base superalloy strengthened by the solid solution strengthening effects of Cr and Mo and the precipitation hardening effects of gamma-prime and carbides. The alloy finds wide-ranging applications at high temperatures in aircraft ducting systems, gas-turbine flame tubes, missile hot components, superheater tubes and nuclear reactors as wrapper tubes, clad tubes and tie rods. Some information exists in literature on tensile properties, but it is relatively scanty on fatigue and creep-fatigue properties. An attempt is made in this work to understand the influence of prior microstructure on the deformation and fracture behaviour of this alloy at high temperatures.

2. Experimental procedure

Low-cycle fatigue tests were performed in air under axial strain-controlled mode using servohydraulic systems on specimens of 25- and 10-mm gauge length and diameter. Three different microstructural conditions investigated were developed by suitable heat treatments. Alloy A was in solution annealed condition devoid of all carbides and gamma-prime of 18 nm diameter and $M_{23}C_6$ precipitates; Alloy C was also in double-aged condition with gamma-prime of 35-nm diameter and MC and $M_{23}C_6$ precipitates. The effect of prior microstructure and strain amplitude of the LCF properties of the alloys was investigated at 923 K at a constant strain rate of 3×10^{-3} s^{-1}. The effect of strain rate on the LCF properties of alloys A and B was examined at three temperatures, namely, 723, 823 and 923 K at a fixed strain amplitude of ±0.6%. Optical microscopy, scanning electron microscopy and transmission electron microscopy of fatigue-tested samples were carried out and the deformation processes analysed by a rigorous work-hardening analysis.

3. Results and discussion

The cycle stress responses of alloys A, B and C at 923 K exhibit an initial hardening followed by a softening regime. Figure 1 typically represents such a cycle stress response of alloy B at 923 K. The operative deformation mechanisms depends on the size of the gamma-prime: shearing for fine and Orowan looping for coarse precipitates. In alloy C, microscopic evidences have been obtained for shearing of the fine gamma-prime formed during testing. Furthermore, the absence of cyclic softening regimes at 300 and 723 K where *in-situ* precipitation does not take place has led to the conclusion that softening in alloy C is associated with the shearing of the fine gamma-prime formed during testing. From a systematic measurement of the slip band spacings on the alloys tested at different strain amplitudes, it has been found that with increase in strain the slip spacing decreases and larger strains are accommodated by an increase in the number density of slip bands. Further, the degree of homogeneity of slip is found to be maximum in alloy A, whereas it is minimum in alloy C. The degree of homogeneity of deformation is found to have a close relationship with the observed fracture modes in alloys A, B and C. Alloy A, possessing the maximum homogeneity in slip, has exhibited transgranular crack initiation and propagation. Alloy B at low strains and alloy C at all strain amplitudes have shown mixed-mode propagation. The impingement of planar slip bands on the grain boundaries in alloys B and C has led to a decohesion of the carbide–

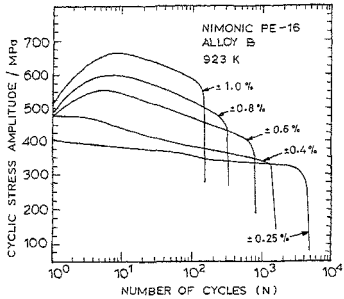

FIG. 1. Cyclic stress response of alloy B at 923 K

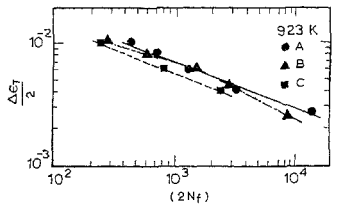

FIG. 2a. Total strain amplitude *vs* number of reversals to failure.

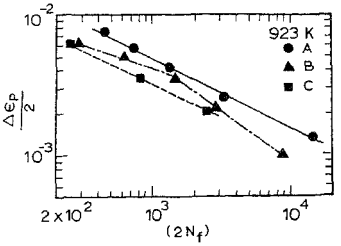

FIG. 2b. Coffin–Manson plots of alloys A, B, and C at 923 K.

matrix interface and intergranular cracks. These variations in deformation homogeneity and fracture modes have resulted in the difference in fatigue life of the alloys (Fig. 2). The superior fatigue resistance of alloy A is attributed to the beneficial effects associated with the reversibility of slip and observed increase in the degree of slip homogeneity. In alloy C, *in-situ* precipitation leads to strain localization and internal cracks. Furthermore, the occurrence of intergranular cracks associated with grain boundary carbides resulted in poor fatigue life of alloy C.

The dependence of cyclic stress-response behaviour and fatigue life on strain rate and prior microstructure has been analysed in detail and mechanisms responsible for them are examined. Furthermore, the dynamic strain ageing (DSA) characteristics in LCF of alloy A have been established by conducting exploratory fatigue tests.

The initial hardening seen in cyclic stress response has been attributed to the dislocation–dislocation interactions at a strain rate of 3×10^{-2} s^{-1}. At low strain rates, at 723 and 823 K, DSA influences dislocation motion and work hardening. Type A+B serrations are observed in low temperature regimes and Type C serrations at $T \geq 723$ K. Furthermore, plateaux in the yield stress and a positive temperature dependence of flow stress are observed in the DSA temperature range. Applying McCormick's model over the temperature range where positive Portevin Le Chatlier effect is observed, the activation energy for the onset of serrated flow is obtained as 258 kJ/mole. DSA has been attributed to the locking of mobile dislocations by substitutional elements, Al and Ti. At all temperatures, with increase in strain rate from

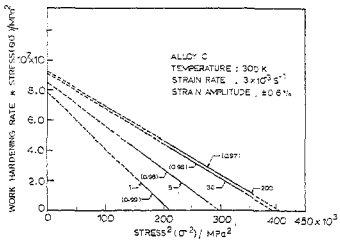

FIG. 3. Variation of $\theta\sigma$ with σ^2 (numbers in brackets indicate correlation coefficient)

3×10^{-5} s^{-1}, fatigue life increases and reaches a peak value at intermediate strain rates. However, with further increase in the strain rate life decreases. From slip band spacing measurements the high fatigue life at intermediate strain rate has been found to be associated with the maximum degree of homogeneity in deformation. At low strain rates DSA enhances the localization of deformation and causes intergranular cracks. However, at 923 K, at low strain rates, oxidation influences fatigue fracture and decrease fatigue life.

The mechanisms associated with cyclic hardening and softening have been analysed from the tensile portions of the hysteresis loops using Kocks–Mecking–Estrin's (KME) models[1]. In alloy C at 300 and 723 K, the applicability of the modified KME model has been established from a linear variation of $\theta\sigma$ with σ^2. Figure 3 represents a typical example of $\theta\sigma$–σ^2 plot seen in alloy C at 300 K. Here, the ordinate intercept which is inversely proportional to interparticle spacing increases with successive cycles. A physical process that can explain the phenomenon is the formation of Orowan loops. As each dislocation leaves a loop around the particle, the effective interparticle spacing decreases. A similar analysis of the models in alloy B revealed that linearity of $\theta\sigma$–σ^2 plots holds good for successive cycles. The ordinate intercept increases in the hardening regime while it decreases in the softening regime. A physical process that can explain the phenomenon is the formation of pile-ups on gamma-prime in the hardening cycles. As shearing starts, effective mean free path of the mobile dislocations increases due to a reduction in the precipitate size. Furthermore, in alloy A, at 3×10^{-2} s^{-1} at 823 K a linear variation of $\theta\sigma$ with σ^2 plots indicates the applicability of the modified KME model and obstacles to the dislocation motion are considered to be slip band intersections.

4. Conclusions

a) Under a suitable combination of prior microstructure and testing temperature, the cyclic stress responses of the alloys are marked by an initial hardening followed by a softening regime. Hardening is mainly due to dislocation/dislocation and dislocation/precipitate interaction while softening is due to a reduction in the size of the gamma-prime due to repeated shearing.

b) Modified Kocks–Mecking–Estrin's model is found to satisfactorily explain work hardening behaviour of the alloys.

c) Alloy A having the maximum homogeneity in deformation exhibits transgranular crack initiation and propagation and maximum fatigue life, while alloy C having the maximum heterogeneity in deformation shows mixed propagation and minimum fatigue life.

d) At 723 and 823 K, at low strain rates, DSA influences deformation and fracture behaviour and reduces fatigue life. At 923 K, oxidation enhances transgranular and intergranular crack initiation and propagation and thereby decreases fatigue life.

Reference

1. ESTRIN, Y. AND MECKING, H. *Acta Metall.*, 1984, **32**, 57–70.